



Practical Uncertainties in the Limited Predictability of the Record-Breaking Intensification of Hurricane Patricia (2015)

ROBERT G. NYSTROM AND FUQING ZHANG^a

Department of Meteorology and Atmospheric Science, and Center for Advanced Data Assimilation and Predictability Techniques, The Pennsylvania State University, University Park, Pennsylvania

(Manuscript received 2 January 2019, in final form 24 June 2019)

ABSTRACT

Hurricane Patricia (2015) was a record-breaking tropical cyclone that was difficult to forecast in real time by both operational numerical weather prediction models and operational forecasters. The current study examines the potential for improving intensity prediction for extreme cases like Hurricane Patricia. We find that Patricia's intensity predictability is potentially limited by both initial conditions, related to the data assimilation, and model errors. First, convection-permitting assimilation of airborne Doppler radar radial velocity observations with an ensemble Kalman filter (EnKF) demonstrates notable intensity forecast improvements over assimilation of conventional observations alone. Second, decreasing the model horizontal grid spacing to 1 km and reducing the surface drag coefficient at high wind speed in the parameterization of the sea surface-atmosphere exchanges is also shown to notably improve intensity forecasts. The practical predictability of Patricia, its peak intensity, rapid intensification, and the underlying dynamics are further investigated through a high-resolution 60-member ensemble initialized with realistic initial condition uncertainties represented by the EnKF posterior analysis perturbations. Most of the ensemble members are able to predict the peak intensity of Patricia, but with greater uncertainty in the timing and rate of intensification; some members fail to reach the ultimate peak intensity before making landfall. Ensemble sensitivity analysis shows that initial differences in the region beyond the radius of maximum wind contributes the most to the differences between ensemble members in Patricia's intensification. Ensemble members with stronger initial primary and secondary circulations beyond the radius of maximum wind intensify earlier, are able to maintain the intensification process for longer, and thus reach a greater and earlier peak intensity.

1. Introduction

Hurricane Patricia (2015) was an extraordinary storm in the eastern North Pacific basin that underwent an unprecedented rapid intensification (RI) process in which it intensified from a tropical storm, with maximum wind speeds of 30 m s^{-1} , to a category 5 hurricane, with maximum wind speeds of 95 m s^{-1} , in less than 36 h. While tropical cyclone (TC) track forecasts have been improving substantially over recent decades, and intensity forecast have also improved some in recent years (Cangialosi 2018), Hurricane Patricia set records for maximum eastern North Pacific NHC official intensity forecast errors at 12, 24, 36, and 48 h lead times

(Kimberlain et al. 2016). Additionally, no operationally available dynamical or statistical guidance was able to correctly forecast the peak intensity or rate of intensification. In this study, we demonstrate methods for improved prediction of Hurricane Patricia using a cycling ensemble data assimilation system and also examine potential sources of model and initial condition (IC) uncertainties that can limit the predictability of intense tropical cyclones, even when the environmental conditions are favorable.

Hurricane Patricia's complete life cycle is well described in Kimberlain et al. (2016), and the records that Patricia set are listed in Rogers et al. (2017). Only a brief summary will be provided here. Hurricane Patricia developed into a tropical depression by 0600 UTC 20 October, as a result of a complex interaction between large-scale forcing (e.g., rising branch of the Madden-Julian oscillation and deep convection coupled with a Central American gyre) and mesoscale processes

^aDeceased.

Corresponding author: Robert G. Nystrom, rnystrom@psu.edu

including a localized gap wind event (Kimberlain et al. 2016; Bosart et al. 2017). Patricia reached tropical storm intensity 18 h after becoming a tropical depression, eventually becoming a hurricane 24 h later, near 0000 UTC 22 October. At this time, Patricia was located in a very favorable environment with anomalously warm ocean temperatures, weak vertical wind shear, and moist atmospheric conditions (Kimberlain et al. 2016). Undergoing a dramatic and record-setting RI of 54 m s^{-1} in a 24 h period (Rogers et al. 2017), Patricia reached its estimated peak intensity with wind speeds of 95 m s^{-1} , less than 36 h after being designated as a hurricane. Hurricane Patricia, however, was not done setting records as it rapidly weakened by 26 m s^{-1} in only 5 h—the most rapid overwater weakening rate on record (Rogers et al. 2017)—prior to landfall along the southwestern Mexico coast, shortly before 0000 UTC 24 October (Kimberlain et al. 2016).

One factor believed to have been especially important in allowing Patricia to set records in terms of intensification rate and peak intensity was the anomalously warm sea surface temperatures (SSTs) present along Patricia's track (e.g., Foltz and Balaguru 2016; Huang et al. 2017; Rogers et al. 2017; Fox and Judt 2018). Hurricane Patricia occurred during a strong El Niño, in which SSTs were more than 1°C warmer than the climatological average (Foltz and Balaguru 2016) and in the 99th percentile for all eastern North Pacific hurricanes (Fox and Judt 2018).

Recent works investigating the practical and intrinsic predictability of TCs (e.g., Sippel and Zhang 2008; Hakim 2013; Brown and Hakim 2013; Kieu and Moon 2016; Judt et al. 2016; Torn 2016; Finocchio and Majumdar 2017) have not only greatly increased our understanding of their chaotic dynamic processes and helped lead to improved intensity prediction, but also indicated that TCs may have higher predictability in certain regimes (e.g., Zhang and Tao 2013; Tao and Zhang 2014). Zhang and Tao (2013) demonstrated using idealized simulations of TCs under various vertical wind shear conditions that TCs under weak vertical wind shear are more intrinsically predictable than TCs under moderate vertical wind shear. Additionally, Tao and Zhang (2014) demonstrated that TCs in the presence of warmer ocean waters intensified earlier and exhibited greater intrinsic predictability of RI compared to TCs over cooler ocean waters. Weak vertical wind shear and a warm ocean surface well describe the environmental conditions present when Patricia rapidly intensified, as the average along-track SSTs and vertical wind shear were in the 99th and 17th percentile, respectively, for all eastern North Pacific hurricanes (Fox and Judt 2018). Based on this we may expect an

increased predictability of Patricia's RI relative to other RI events and indeed this is speculated by Fox and Judt (2018), where they demonstrate small changes to RI forecasts of Patricia when very small perturbations are applied to a control simulation. Additionally, Qin and Zhang (2018) also hypothesized that favorable large-scale environmental conditions may have made Patricia's intensification more predictable. However, the substantial gap between the expected high intrinsic predictability—given the favorable environmental conditions—and the actual low practical predictability of Patricia's intensity from operational real-time forecasts presents an apparent contradiction and will be explored within this study.

Given the large errors by all forecast models in Patricia's intensification and peak intensity, and given the large divergence among operational forecast guidance, the current study focuses on key uncertainties that may have limited the practical aspects of the predictability of Patricia—despite favorable environmental conditions that may potentially allow high intrinsic predictability. Key limiting factors potentially include but are not limited to: data assimilation methodology and the availability and quality of observations (e.g., Zhang et al. 2004; Torn and Hakim 2009; Weng and Zhang 2012; Majumdar et al. 2013; Zhang and Pu 2014; Poterjoy et al. 2014; Aberson et al. 2015; Zhang and Weng 2015; Poterjoy and Zhang 2016), model resolution and physics (e.g., Davis et al. 2008; Jin et al. 2014; Judt et al. 2016; Torn 2016; Melhauser et al. 2017; Qin and Zhang 2018), the underlying inner-core TC dynamics (e.g., Van Sang et al. 2008; Hakim 2013; Brown and Hakim 2013; Torn and Cook 2013; Judt et al. 2016; Emanuel and Zhang 2016; Kieu and Moon 2016; Torn 2016; Finocchio and Majumdar 2017; Nystrom et al. 2018), and the environmental conditions (e.g., Torn and Cook 2013; Judt et al. 2016; Emanuel and Zhang 2016; Torn 2016; Nystrom et al. 2018).

In this study we focus on just a few factors from the above list, which were identified as key factors limiting the practical predictability of Patricia. First, we are particularly interested in the impact of realistic IC uncertainties represented by posterior analysis perturbations resulting from a state-of-the-art ensemble data assimilation system on Patricia's prediction. Second, given the observed small inner core of Patricia, we examine the implications of the model horizontal resolution, which is often limited by computational cost, on the accuracy and predictability of Patricia's intensification. Last, motivated by the large uncertainty in the physics related to the air–sea fluxes at high wind speeds (e.g., Powell et al. 2003; Hsu et al. 2017), we examine the impact of surface flux parameterization uncertainty on the prediction of Patricia's intensification.

The remainder of the paper is organized as follows. Section 2 will describe the methodology used. Section 3 will present the main findings from data assimilation experiments, high-resolution ensemble forecasts, and potential model errors that were found to meaningfully impact the practical predictability. Section 4 will provide the concluding discussions.

2. Methodology

a. Cycling PSU WRF EnKF data assimilation system

In this study, we utilize a modified version of the PSU WRF EnKF real-time system for hurricane analysis and prediction (Zhang and Weng 2015; Weng and Zhang 2016), utilizing WRF version 3.5.1 (Skamarock et al. 2008), to investigate the potential for improving prediction of Hurricane Patricia (2015). The initial and boundary conditions of the 60-member ensemble were interpolated from the Global Forecast System (GFS) operational analysis at 0000 UTC 21 October, with added ensemble perturbations generated by the background error covariance (CV3 option) (Barker et al. 2004). The ensemble is then run for 12 h to spin up the flow-dependent ensemble background error covariance at the convection-permitting resolution. The cycling ensemble data assimilation begins at 1200 UTC 21 October. Two EnKF analysis experiments are performed in this study. The first, “CONV,” assimilates hurricane position and intensity (HPI) observations and all conventional observations in the Global Telecommunication System (GTS) data stream (available from the NCAR RDA). The second, “Airborne+CONV,” assimilates airborne radial velocity super observations, similar to Weng and Zhang (2012), in addition to the observations in CONV. Super observations are created in real time at the NOAA Hurricane Research Division based on the methodology described in Weng and Zhang (2012, 2016). Briefly, super observations are created by averaging radial velocity observations, obtained from forward and backward scans from the NOAA P-3 Tail Doppler Radar, within a trapezoid that is 5 km in the radial direction by 5° in the azimuthal direction.

One modification to the PSU WRF EnKF real-time system is that the data assimilation cycles are performed at an hourly frequency in this study to limit the prior position spread among the ensemble members that can lead to an unrealistically weak storm in the (Eulerian) ensemble mean, in particular since the inner core size of Patricia is very small. More frequent EnKF cycling has also been recommended by Chen and Snyder (2007) and others, primarily to prevent the vortex position spread from becoming too large such that background errors likely become far from a Gaussian distribution, a

critical assumption of the EnKF method used for data assimilation. Additionally, this study uses covariance inflation through relaxation to prior perturbation (Zhang et al. 2004), but a smaller alpha value of 0.5 is used for the inner core region of the storm vortex (within 300 km of the best track center) than for the environment (greater than 600 km from the best track center), where the alpha value is 0.75. A distance weighted linear combination is used between 300 and 600 km to gradually transition from the inner-core alpha value to the environment alpha value. The alpha equal to 0.5 used in RTPP within 300 km of the best track TC location means that we relax our posterior perturbations 50% toward the prior perturbation, as compared with 75% in the environment (beyond 600 km) where alpha is 0.75. This results in smaller posterior ensemble spread within 300 km as opposed to using a uniform alpha of 0.75 everywhere. The difference in alpha values utilized between the region of the storm vortex and the environment is a result of the more rapid ensemble spread growth within the inner core region, as a result of both inner-core dynamical processes and ensemble position spread with very tight gradients in many state variables (e.g., winds and pressure).

The WRF Model for the cycling EnKF system is configured otherwise similar to the real-time PSU WRF EnKF system with three two-way nested domains with horizontal grid spacing of 27, 9, and 3 km. Domain configuration and parameterization schemes are nearly identical to Zhang and Weng (2015), except that the domains have been shifted to be focused over the eastern North Pacific, where the outermost domain covers a region from 10°S–45°N to ~150°–50°W, and the surface flux parameterization for the air–sea enthalpy and momentum exchange has been changed to that from Chen et al. (2018), where the surface drag coefficient decreases with wind speed for winds greater than hurricane force (33 m s⁻¹). The change to the surface flux parameterization is more consistent with recent modeling advances (e.g., Chen et al. 2018), in which it is indicated that the surface drag coefficient does not continue to increase with wind speed beyond hurricane force.

Deterministic forecasts are initialized from the EnKF analysis mean with an additional nested domain (297 × 297 grid points) centered on the storm with 1-km horizontal grid spacing throughout the entirety of the forecast. The deterministic forecasts thus utilize four two-way nested domains in which the innermost three domains follow the storm. Deterministic forecasts are initialized every 6 h beginning at 1200 UTC 21 October–1800 UTC 22 October, with an additional deterministic forecast initialized at 2100 UTC 21 October immediately following the first NOAA P-3 flight through

Patricia. A total number of seven deterministic forecasts are conducted for Patricia and each forecast is run through 1200 UTC 24 October, which is ~ 12 h after Patricia's landfall.

b. TCI dropsonde observations and best track intensity and track verification

For verification of the EnKF analysis, as well as the forecasts, both best track estimates for position and intensity and high-density dropsonde observations from the Tropical Cyclone Intensity (TCI) field experiment (Bell et al. 2016; Doyle et al. 2017) are utilized. The best track, from HURDAT2 and linearly interpolated to hourly intervals, is used to verify the storm position, maximum wind speed, and minimum central pressure. The TCI dropsondes allow for the verification of the EnKF analysis and model forecasted storm structure using independent observations that are not assimilated. The verification of the storm's kinematic and thermodynamic structure is conducted using the TCI dropsondes by analyzing the storm-relative azimuthally averaged structure, or the observations within a storm-relative radius/height framework.

Following Stern and Zhang (2016) and Munsell et al. (2018), the dropsonde observations for a given flight are binned by radii within 2-km-wide bins at each vertical level, as the sonde descends, based on the NOAA Hurricane Research Division wind center track at the release time of each drop (http://www.aoml.noaa.gov/hrd/Storm_pages/patricia2015/patricia.trak). A simple cubic interpolation is utilized for any regions of missing values and Gaussian smoothing is applied to remove some of the noise.

c. Maximum potential intensity

In this paper, we calculate the maximum potential intensity using the following:

$$V_m^2 = \frac{T_s C_k \{V_m\}}{T_o C_d \{V_m\}} (\text{CAPE}^* - \text{CAPE})|_m, \quad (1)$$

which is modified slightly from Emanuel (1995), where V_m is the maximum gradient wind speed, T_s is the SST, T_o is the outflow temperature, C_k is the enthalpy exchange coefficient and is now a function of V_m , C_d is the drag coefficient and is also now a function of V_m , CAPE^* is the convective available potential energy of a saturated parcel lifted from the surface, and CAPE is the convective available potential energy of a parcel lifted from the surface. The outflow temperature T_o is calculated here as the temperature at the level of neutral buoyancy, where the level of neutral buoyancy is determined by calculating the CAPE of a parcel lifted from

the surface. Using (1), the maximum theoretical potential wind speed is calculated for each point in domain 2, using the C_k - C_d relationship used by the model during forward integration, and is the average of the maximum potential wind speed for all points within 50 km of the simulated storm's position at a given forecast time. Because C_k and C_d change with the calculated V_m , an iterative method is used in which C_k and C_d are calculated based on V_m . This process is repeated until convergence of V_m occurs. (Besides the modifications to C_k and C_d , this calculation is identical to as done for the real-time maps of potential intensity shown at <http://wxmaps.org/pix/hurpot>.)

3. Results and discussion

a. Sensitivity of Patricia's prediction to the assimilation of airborne inner-core observations

Operational guidance, such as HWRF, and official NHC forecasts for Hurricane Patricia had intensity forecast errors in excess of 30 m s^{-1} (Figs. 1a-c)—including official forecast errors that were the highest on record for the eastern North Pacific basin (Kimberlain et al. 2016). Ensemble data assimilation experiments are conducted to investigate potential improvements from assimilation of conventional observations (CONV) and airborne radial velocity observations (Airborne+CONV). For each cycling ensemble data assimilation experiment, observations are assimilated hourly between 1200 UTC 21 October and 1800 UTC 22 October and deterministic forecasts with 1-km horizontal grid spacing are initialized from the EnKF analysis mean every 6 h or immediately following assimilation of airborne radial velocity observations (2100 UTC 21 October). Following assimilation of airborne radial velocity observations, the ensemble spread in initial minimum central pressure and maximum surface wind speed is reduced by 2.1 hPa and 2.4 m s^{-1} ($\sim 50\%$), relative to CONV (not shown). Both the 1-km deterministic intensity forecasts from CONV (Figs. 1d-f) and Airborne+CONV (Figs. 1g-i), outperform the operational intensity guidance and official forecasts (Figs. 1a-c). This is likely from a combination of improved ICs, resulting from improved data assimilation, and reduced model errors, including model horizontal resolution and/or differences in model dynamics and physics. While both CONV and Airborne+CONV demonstrate substantial improvement over NHC operational guidance in terms of capturing the record observed peak intensity, the timing of reaching the observed peak intensity is much improved in Airborne+CONV (e.g., within 1 h for forecast initialized from 2100 UTC 21 October) as compared to CONV

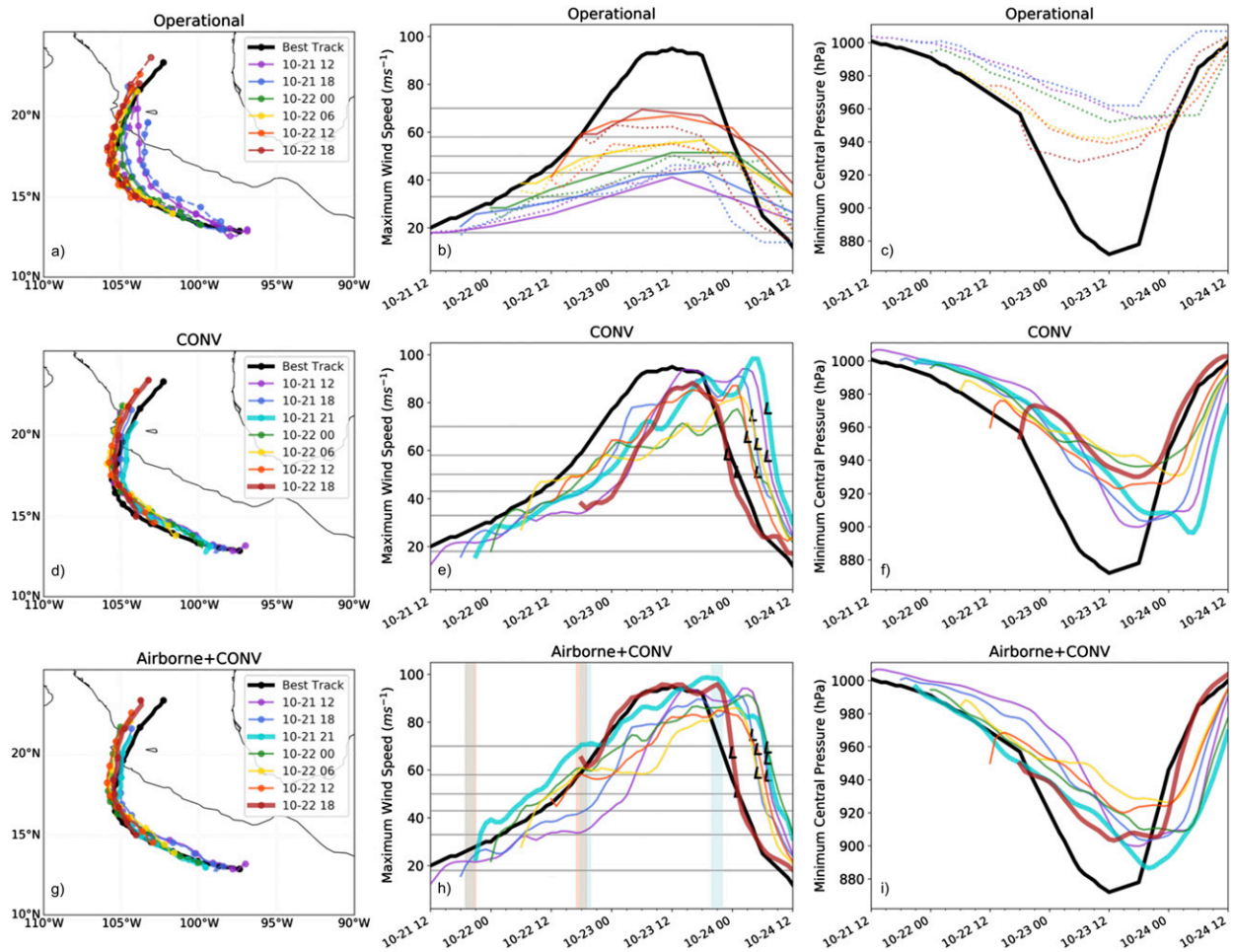


FIG. 1. (top) Real-time operational guidance, HWRF (dashed) and NHC official forecasts (solid), (middle) deterministic WRF forecasts from assimilation of conventional observations only, and (bottom) deterministic WRF forecasts from assimilation of conventional observations plus P-3 Doppler radial velocity super observations. Both sets of deterministic WRF forecasts utilize 1 km horizontal grid spacing for the innermost domain. The WRF forecasts initialized immediately following P-3 flights through Patricia (2100 UTC 21 Oct and 1800 UTC 22 Oct) appear as thicker lines. Solid gray horizontal lines on the corresponding maximum wind speed panels denote the cutoffs on the Saffir–Simpson hurricane wind scale. (left) Markers on the track lines denote position every 6 h and (middle) “L”s on intensity forecast denote landfall timing. Red and blue shaded periods denote the time periods of P-3 and TCI observations, respectively.

(e.g., 15 h delayed for forecast initialized from 2100 UTC 21 October), likely a result of the improved analysis of the structure of Patricia as will be further discussed.

There is a large overprediction in maximum surface winds after \sim 1800 UTC 23 October for many of the deterministic forecasts because the landfall timing is delayed relative to observations, but once the correct landfall timing is more accurately captured (e.g., 1800 UTC 22 October), the timing of rapid weakening is also better captured. We speculate that the observed secondary eyewall (Rogers et al. 2017)—which is simulated in some of our deterministic forecasts (not shown)—may also have contributed to the weakening of the storm prior to landfall. Additionally, Martinez et al. (2019) suggest that eddy mixing processes may have

been a primary cause of Patricia’s rapid overwater weakening.

To examine the reasoning for the improved deterministic forecasts in Airborne+CONV, the structure of the EnKF analysis mean from CONV and Airborne+CONV from 2100 UTC 21 October and 1800 UTC 22 October are each examined and compared with high density dropsonde observations from the TCI field campaign (Doyle et al. 2017) obtained between 1855 and 2040 UTC 21 October and 1746 and 1945 UTC 22 October that were not assimilated. The EnKF analysis from Airborne+CONV results in a considerably improved structure compared to CONV and a better match to these independent observations (Figs. 2 and 3a–c). As seen in the observations near 2100 UTC

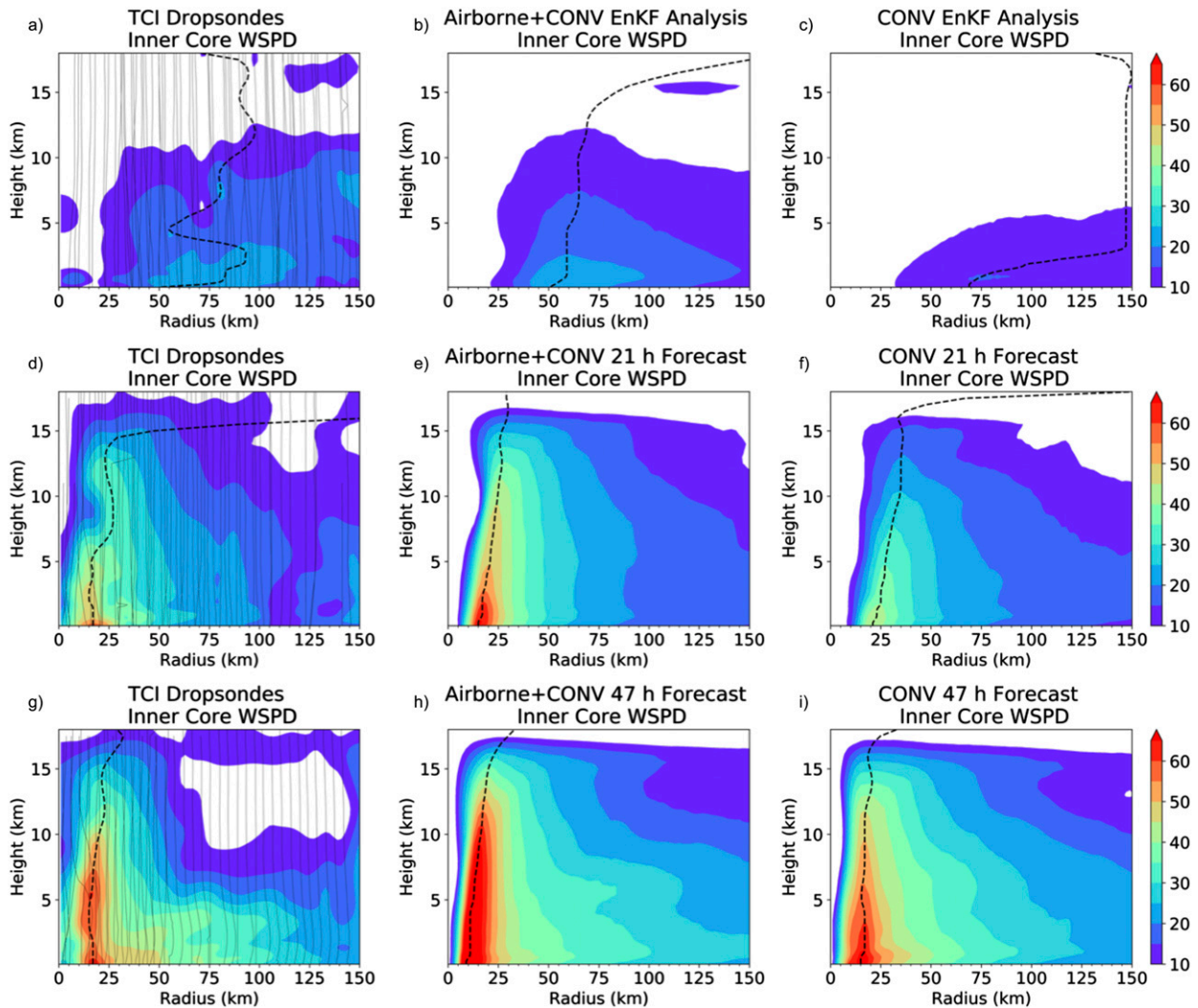


FIG. 2. Comparison of storm-relative radius–height structure of wind speed in m s^{-1} between (left) TCI dropsonde observations from NASA WB-57, (middle) Airborne+CONV EnKF analysis mean or forecast, and (right) CONV EnKF analysis mean or forecast from 2100 UTC 21 Oct. Dropsonde trajectories are shown by gray lines on the plot of dropsonde wind speeds. The RMW is denoted by the dashed black line.

21 October, a vortex with wind speeds greater than 20 m s^{-1} is captured in Airborne+CONV and a radius of maximum wind (RMW) near 50 km is also seen, which is not the case for CONV (Figs. 2a–c). Similarly, for the analysis at 1800 UTC 22 October the Airborne+CONV analysis better matches with the TCI dropsondes than that of CONV (Figs. 3a–c).

After 21 h into the deterministic forecasts from the 2100 UTC EnKF Analysis, which is in the middle of RI, the TC in Airborne+CONV is stronger in terms of maximum wind speed, has a smaller RMW ($\sim 15 \text{ km}$), and is more similar to TCI dropsonde observations—in terms of the maximum wind speed, RMW, and overall vertical structure of the TC—than CONV (Figs. 2d–f). At 47 h, shortly ($\sim 8 \text{ h}$) after the peak estimated intensity,

both Airborne+CONV and CONV result in very strong storms, but Airborne+CONV is still stronger than CONV (Figs. 2g–i). Similar results are seen for the forecasts initialized from the 1800 UTC 22 October analysis (Figs. 3d–f). Additionally, Airborne+CONV has a broader wind field than CONV and is more similar to observations—in terms of the radial structure—especially beyond 50 km from the storm center (Figs. 2 and 3). Airborne+CONV also develops a secondary eyewall, similar to what is seen in observations, unlike CONV (not shown). Overall, while differences between dropsonde observations and the deterministic forecasts initialized at 2100 UTC 21 October and 1800 UTC 22 October exist, the forecasts initialized from the Airborne+CONV EnKF analysis have a

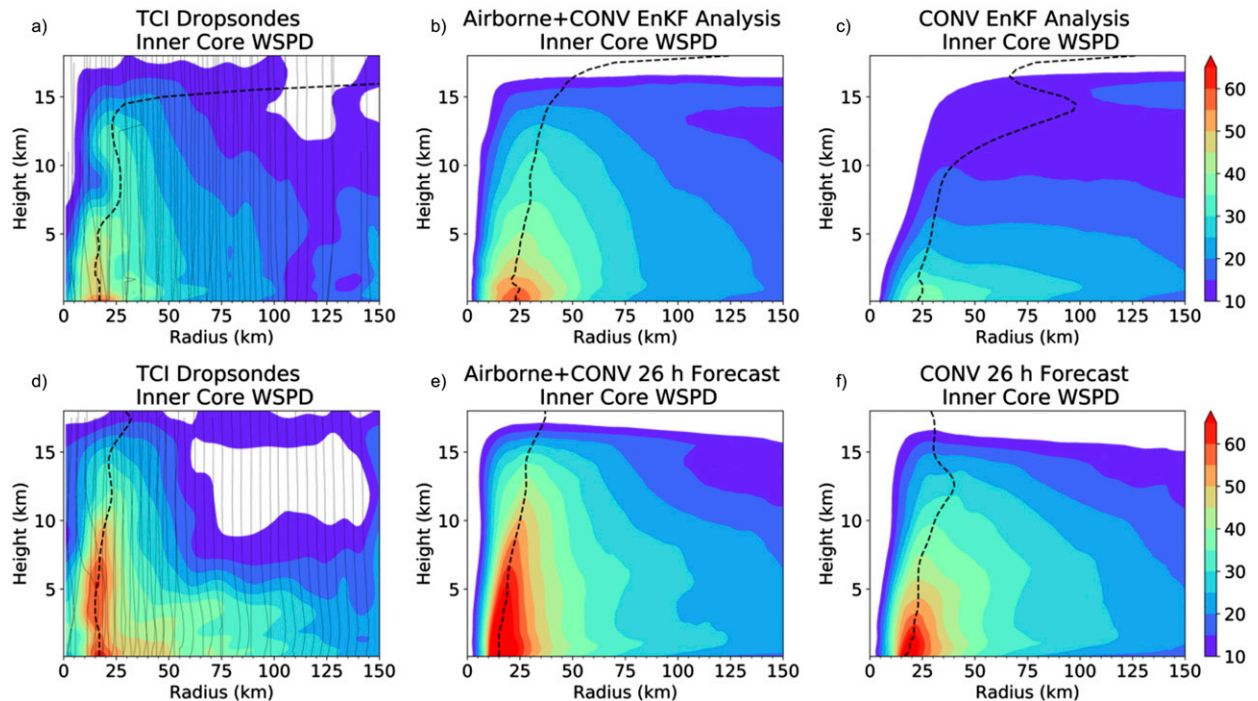


FIG. 3. As in Fig. 2, but for the 1800 UTC 22 Oct EnKF analysis.

much-improved representation of the size and intensity evolution of Patricia than CONV.

b. Sensitivity of Patricia's rapid intensification to realistic initial condition uncertainties

To better assess the practical predictability of and processes important in Patricia's RI, a 60-member ensemble forecast with 1-km horizontal grid spacing was conducted from the Airborne+CONV EnKF analysis perturbations at 2100 UTC 21 October. The 2100 UTC 21 October initialization was chosen because this analysis time had assimilated all observations from the first NOAA P-3 flight and the deterministic forecast captured Patricia's RI timing and peak estimated wind speed. The 60-member ensemble forecast has many members that successfully capture the peak intensity, in terms of maximum wind speed and the timing and rate of intensification (Fig. 4). On the other hand, a notable number of other members either intensify the storm ~ 12 h delayed or even worse, fail to intensify. Additionally, uncertainty in the timing of landfall appears to result in large intensity uncertainty beyond ~ 42 h.

To examine the predictability of the simulated maximum intensity more quantitatively, probability density functions (PDFs) and cumulative density functions (CDFs) are estimated from the ensemble distributions of peak lifetime maximum wind speed (Fig. 5a) and maximum wind speed at the time of observed maximum

wind speed (39 h; Fig. 5b). An extreme value distribution function is fit to the data for the PDF of peak lifetime maximum wind speed and maximum wind speed at 39 h. The observed maximum wind speed of 95 m s^{-1} is near the peak of the PDF for both the peak simulated maximum wind speed and the maximum wind speed at 39 h, demonstrating both the peak observed intensity and timing are captured near the center of the ensemble envelope. Additionally, the CDF of simulated peak maximum wind speed indicates a 60% chance of reaching at least the observed maximum wind speed during some period of the forecast, although the ensemble spread in the timing of peak simulated wind speed is 7.5 h. The ensemble probability of reaching the observed peak intensity within 6 h of the correct time is reduced by nearly 20% in comparison to the probability of reaching the observed peak wind speed at any time during the forecast. This indicates that the timing of peak intensity was considerably less predictable than the peak intensity itself. We also note that the time of simulated peak lifetime wind speed is delayed relative to the time observed.

In addition to the record-breaking peak intensity reached, which was well captured within the ensemble forecast envelope, Patricia also underwent an unprecedented 24 (12) h intensification period where its maximum surface wind speed increased by an estimated 54 (33) m s^{-1} (Rogers et al. 2017). The observed 12 and

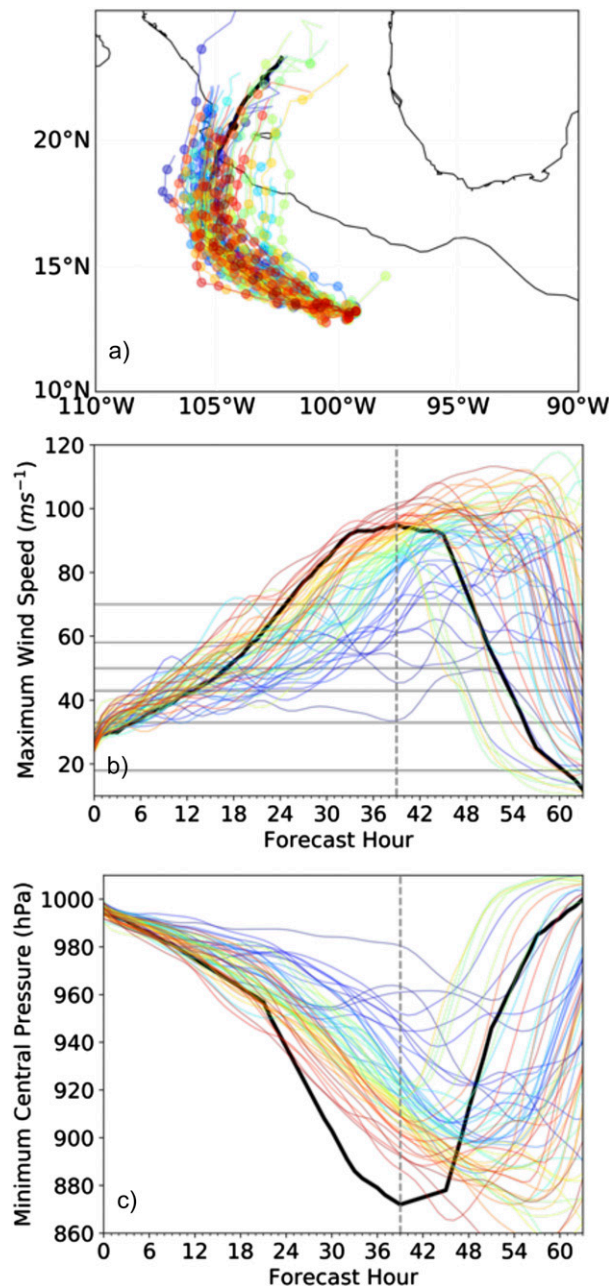


FIG. 4. The 60-member ensemble forecast with 1-km horizontal grid spacing of (a) position, (b) maximum 10 m wind speed, and (c) minimum central pressure. Forecasts were initialized from the Airborne+CONV EnKF analysis at 2100 UTC 21 Oct. Ensemble members are colored relative to their intensity at the time of peak estimated intensity (39 h, time marked with a vertical gray dashed line) with warmer colors being stronger ensemble members at this time and cooler colors being weaker ensemble members. The best track is shown as the black curve.

24 h maximum intensification rates were captured within the ensemble envelope and a Gaussian PDF was fit to the ensemble distribution of intensification rate (Figs. 5c,d).

The observed maximum 12 h intensification rate is very near the ensemble mean 12 h maximum intensification rate (peak of the Gaussian fit PDF; Fig. 5c). The estimated probability of an intensification rate of at least 33 m s^{-1} in a 12 h period is 37%. The observed 24 h intensification rate is also captured by the ensemble but with less confidence and is to the right of the peak in the PDF (Fig. 5d). The ensemble estimated probability of an intensification rate of at least 54 m s^{-1} in a 24 h period is 13%. The reduced ensemble probability of the observed 24 h intensification rate, relative to the 12 h intensification rate, indicates that the intensification rate becomes increasingly less predictable with the length of the intensification period, likely a result of internal dynamics or environmental conditions that can disrupt the rapid intensification process.

As a result of the uncertainty in the timing of intensification and, to lesser extent, the peak intensity across the ensemble, the cause of this uncertainty is examined by separating the ensemble members into two groups based on the maximum wind speed at the time of observed peak intensity (39 h); the 20 strongest ensemble members (20-Strong) and the 20 weakest members (20-Weak). The weakest member (member 31), that fails to intensify much at all, is also highlighted to understand why this member failed to intensify. This methodology is similar to many previous studies including Sippel and Zhang (2008), Nystrom et al. (2018), and others. The initial maximum 10-m wind speed and minimum central pressure is similar across the ensemble (Figs. 4b,c) and is not well correlated to the maximum forecast intensity (not shown). Additionally, all members have less than 10 m s^{-1} of deep layer vertical wind shear (most less than 5 m s^{-1}), high midlevel relative humidity, and very warm SSTs in excess of 30°C (not shown). While the environment of individual ensemble members is generally favorable for intensification, variability in environmental wind shear may partially be responsible for the differing intensity evolutions across the ensemble. However, ensemble correlations between environmental wind shear and peak intensity (not shown) are notably weaker than correlations between initial TC structure and peak intensity. Additionally, small SST variability across the ensemble ($\sim 0.5^\circ\text{C}$) may have partially influenced the peak simulated intensity and intensification rate, although SST differences here appear less important than differences in initial TC structure (not shown).

The azimuthally averaged storm-relative structure is examined to understand how uncertainty in the initial structure of the TC impacted the intensification process and ultimately the peak intensity. At the initial time, the 60-member storm-relative ensemble mean maximum

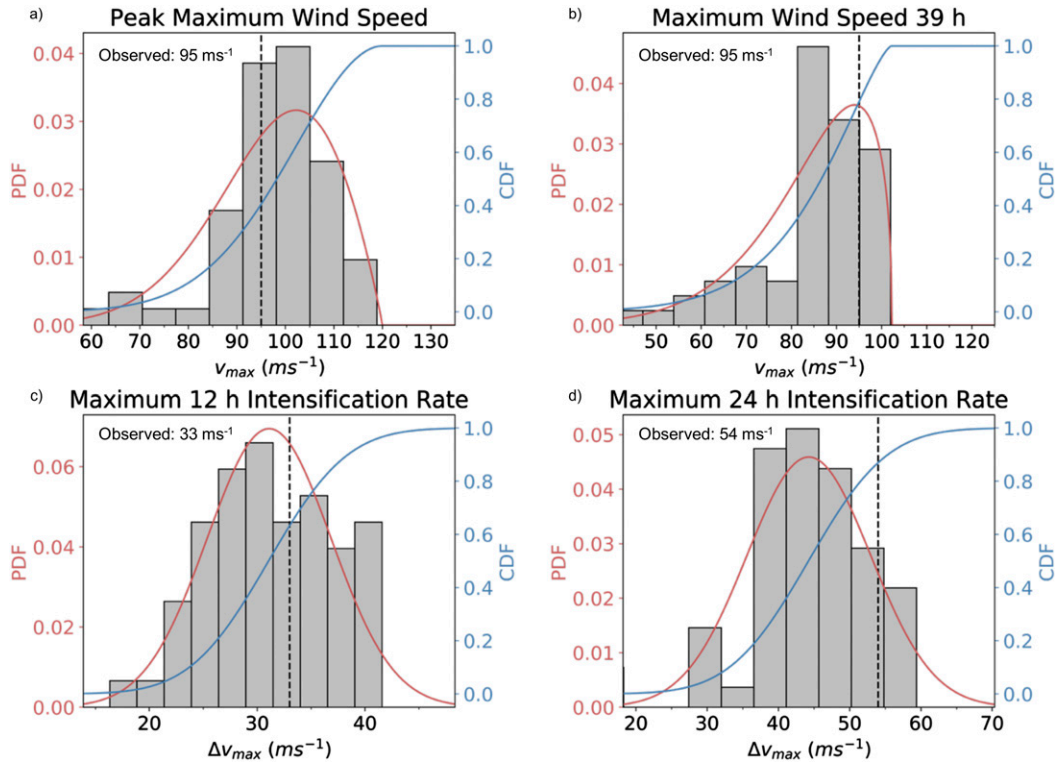


FIG. 5. Ensemble histogram (gray shaded bars), estimated probability density function (red curve), and estimated cumulative density function (blue curve) for (a) forecast peak maximum wind speed, (b) maximum wind speed at the time of time of observed peak intensity (39 h), (c) maximum 12 h, and (d) 24 h intensification rate simulated by the 1-km ensemble forecast shown in Fig. 4. The observed maximum wind speed and intensification rate are depicted by vertical black dashed lines.

tangential wind speed is $20\text{--}25\text{ ms}^{-1}$ with a standard deviation of 2 ms^{-1} and RMW near 50 km at 1-km height (Fig. 6a), in good agreement with the total wind speed and RMW estimated from the TCI dropsonde observations (Fig. 2a). The initial primary circulation of 20-Strong (Fig. 6b) and 20-Weak (Fig. 6c) is similar to the ensemble mean near the RMW, but the tangential wind decreases more rapidly with radius beyond the RMW in 20-Weak. The weakest ensemble member has a similar RMW and maximum wind speed as the ensemble mean, but has a shallower primary circulation and has tangential wind speeds that are weaker than the rest of the ensemble beyond 50 km (Fig. 6d). Overall, the biggest differences between the strongest and weakest ensemble members' primary circulation appear to be beyond $\sim 100\text{ km}$ (~ 2 times of RMW), with the 20-Strong generally having a stronger primary circulation at outer radii. In regards to the secondary circulation, the full ensemble mean has initial low-level inflow in excess of 6 ms^{-1} within the lowest 1 km and upper-level outflow in excess of 8 ms^{-1} near 15 km (Fig. 6e). Similar to the primary circulation, 20-Strong (20-Weak) has an initially stronger (weaker) secondary circulation

(Figs. 6f,g) and the weakest member has the weakest inflow within the boundary layer and outflow in the upper troposphere (Fig. 6h). Directly related to the stronger primary circulation, 20-Strong has greater angular momentum beyond the RMW than 20-Weak, and the weakest member has the smallest angular momentum beyond the RMW (Figs. 6i–l).

By 21 h into the ensemble forecast, the difference in the maximum surface wind speed is evident (Fig. 4b). At this time, the full ensemble storm-relative mean depicts a primary circulation with maximum tangential wind speeds of $45\text{--}50\text{ ms}^{-1}$ and an RMW less than 20 km (Fig. 7a), similar to that depicted by TCI dropsonde observations (Fig. 2d). As seen at the initial time (Fig. 6), 20-Strong has a stronger primary and secondary circulation than 20-Weak and the weakest member vortex still appears much more shallow and weaker overall than 20-Weak (Fig. 7).

Returning to the differences in the ICs that appear to have most significantly impacted the intensification process, storm-relative correlations are calculated between model state variables at the initial time and minimum central pressure at 39 h, the time of observed

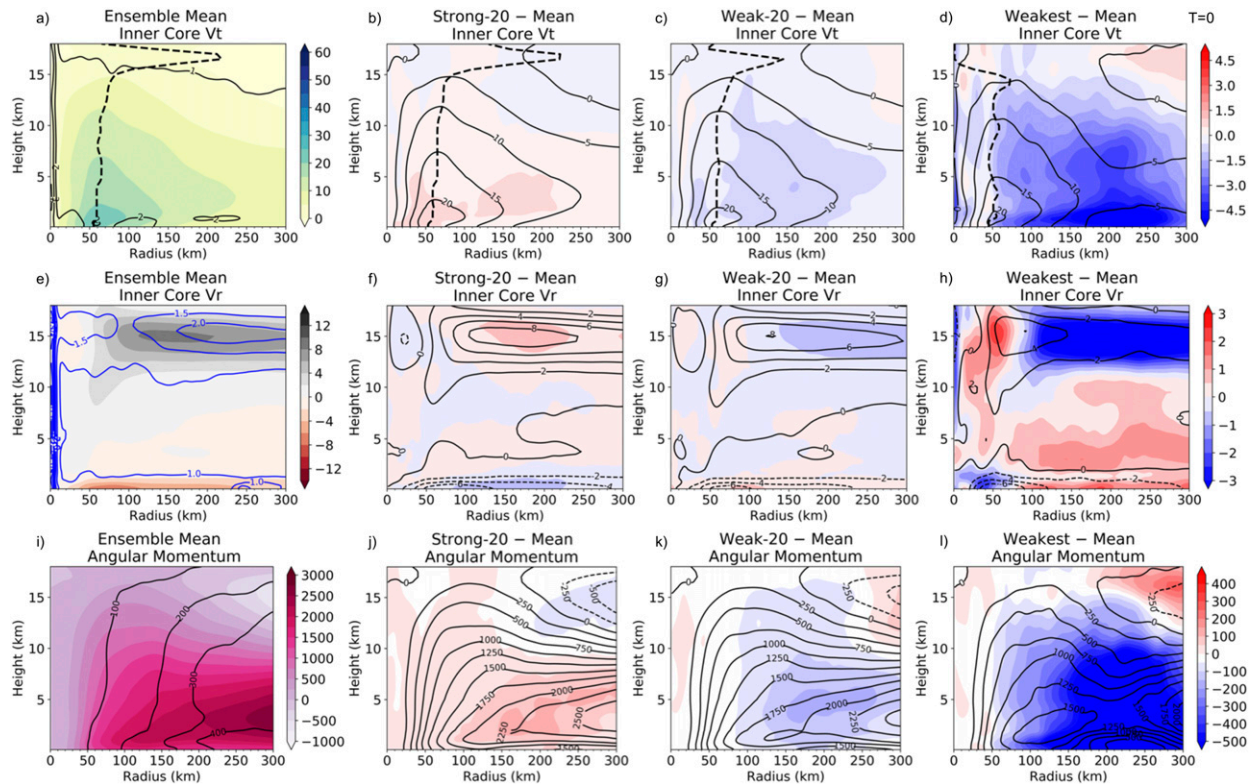


FIG. 6. Comparison of the initial (0h) storm-relative radius–height structure of (a)–(d) tangential wind speed in m s^{-1} , (e)–(h) radial wind speed in m s^{-1} , and (i)–(l) angular momentum in $(10^3) \text{ m}^2 \text{ s}^{-1}$. (a),(e),(i) 60-member ensemble mean (shaded) and ensemble standard deviation (contoured). (columns 2–4) Differences (shaded) between (b),(f),(j) initial mean of the 20 strongest members at 39 h, (c),(g),(k) initial mean of the 20 weakest members at 39 h, and (d),(h),(l) the initial structure of the weakest ensemble member at 39 h and initial 60-member ensemble mean. Also shown in columns 2–4 is the mean quantity of the ensemble subset (contoured) and (top) the RMW (black dashed line).

peak estimated intensity. The largest statistically significant negative correlations between the initial tangential wind speed and the minimum central pressure do not occur at the RMW, but rather in the outer portions of the primary circulation beyond 100 km from the storm center and everywhere below ~ 10 km (Fig. 8a). This indicates that ensemble members with a stronger primary circulation beyond the RMW are more likely to have a lower minimum central pressure at 39 h. Additionally, large correlations appear between the initial secondary circulation and the minimum central pressure at 39 h (Fig. 8b). Positive correlation, greater than 0.4, between the initial radial wind in the lowest ~ 1 km beyond ~ 80 km and the minimum central pressure at 39 h indicates that stronger initial low-level inflow is associated with a stronger TC at 39 h. Similarly, negative correlation, less than -0.4 , between the radial wind above 12 km and minimum central pressure at 39 h indicates that ensemble members with stronger initial outflow were more likely to have a stronger TC at 39 h. Statistically significant negative correlations between initial water vapor mixing ratio (QVAPOR) and minimum central

pressure at 39 h indicate that inner-core moisture may also have played some role in the forecast uncertainty (Fig. 8c), consistent with many previous studies (e.g., Rotunno and Emanuel 1987; Tao and Zhang 2014; Emanuel and Zhang 2017; Nystrom et al. 2018). However, differences here appeared minimal compared to differences in the primary and secondary circulations (not shown) and a moisture swap experiment in which the initial QVAPOR of a bad member (member 31) and the analysis mean are swapped does not meaningfully change the forecast intensity of either (not shown). Finally, a radius–time Hovmöller of ensemble correlation between azimuthal mean 10-m tangential wind speed and the minimum central pressure at 39 h (Fig. 8d) displays strongest negative correlations that propagate inward with time, indicating that initially greater angular momentum available beyond the RMW may have been advected radially inward, helping to spin up the TC.

To further analyze the impact of IC differences within the outer circulation of the storm across the ensemble, as well as environmental IC differences, spatial relaxation

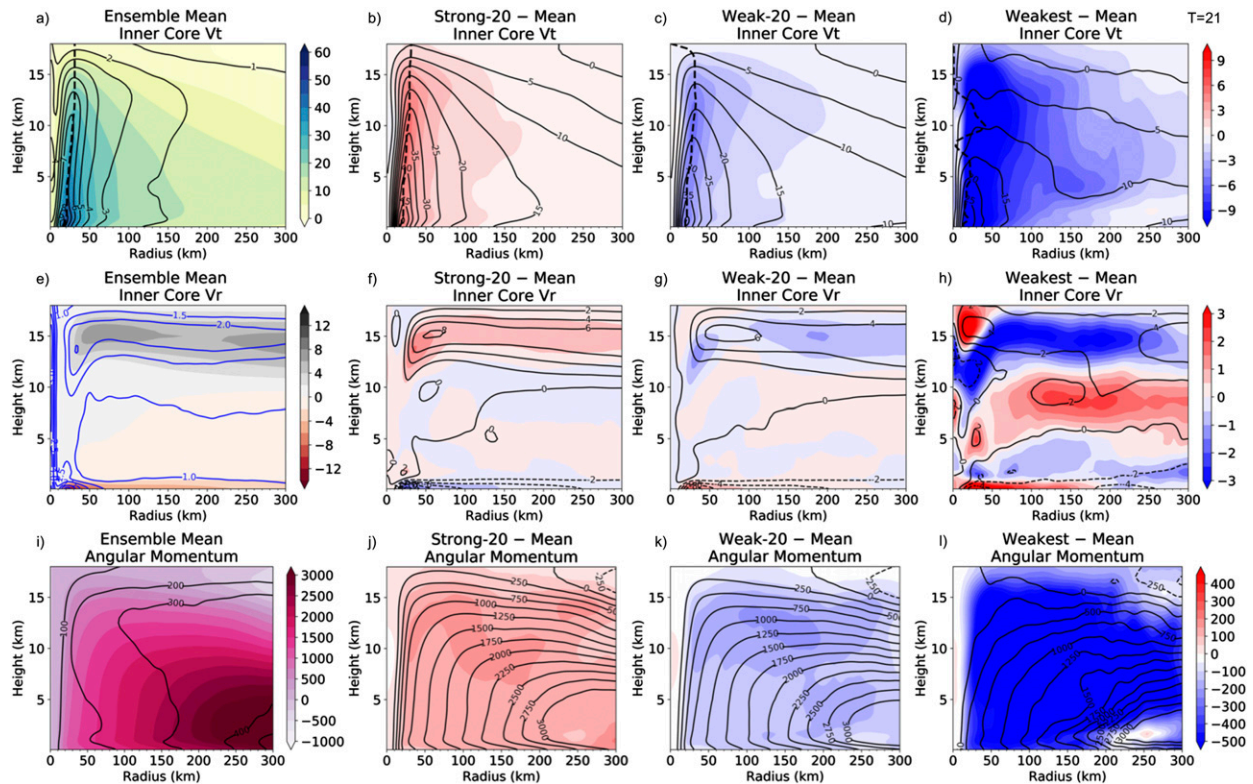


FIG. 7. As in Fig. 6, but for forecast hour 21.

experiments were conducted. These experiments spatially relax either the ICs of the weakest member (31) to the EnKF analysis mean (CNTL) or the EnKF analysis mean (CNTL) to the weakest member (31). The spatial IC relaxation is done through a distance weighted linear combination in which, over a distance of 100 km, ICs of all model state variable are linearly transitioned from member 31 (CNTL) to CNTL (member 31). The relaxation is done within three radii ranges from the TC center: 100–200, 300–400, and 500–600 km. For instance, when ICs from member 31 are linearly transitioned to CNTL from 500 to 600 km (r600mean), the ICs within 500 km are entirely from member 31, the ICs beyond 600 km are entirely from CNTL, and the ICs between 500 and 600 km are a linear distance weighted combination of the two. Two main differences exist between member 31 and CNTL. First, member 31 has greater environmental vertical wind shear than CNTL, defined here as the 850–200 hPa vertical wind shear averaged within an annulus between 200 and 800 km from the storm center, peaking near 9 m s^{-1} at 18 h into the forecast (Figs. 9a,d). Second, the 10-m tangential wind speed within the outer primary circulation, beyond ~ 75 km from the storm center, decreases more rapidly with radius in member 31 compared with CNTL. The initial maximum tangential wind speed is actually a bit

greater and the RMW smaller for member 31 compared with CNTL (Figs. 9b,e).

As the environment becomes more and more like CNTL (e.g., r600mean, r400mean), the vertical wind shear decreases by $\sim 5 \text{ m s}^{-1}$, the storm undergoes a more rapid and earlier intensification and reaches a greater peak intensity (Figs. 9a,c). However, even when the environment, beyond 400 km from the TC center, is from CNTL and the vertical wind shear is decreased to $\sim 4 \text{ m s}^{-1}$, the intensification is still delayed compared to CNTL and the peak maximum wind speed is $\sim 15 \text{ m s}^{-1}$ less than CNTL, indicating that while the increased vertical wind shear in the environmental ICs for member 31 was detrimental to the intensification process it cannot fully explain why the maximum wind speed of this member was $\sim 50 \text{ m s}^{-1}$ weaker than CNTL. When the outer TC circulation of member 31 is gradually relaxed to CNTL between 100- and 200-km radii, the tangential wind speeds are increased within these radii (Fig. 9b) and the intensification timing, rate, and peak intensity are nearly identical to CNTL (Fig. 9c). This result indicates that the breadth and strength of the initial vortex can potentially inhibit the rapid intensification process or, at the very least, delay it—even when environmental conditions are favorable for intensification. This may explain why some

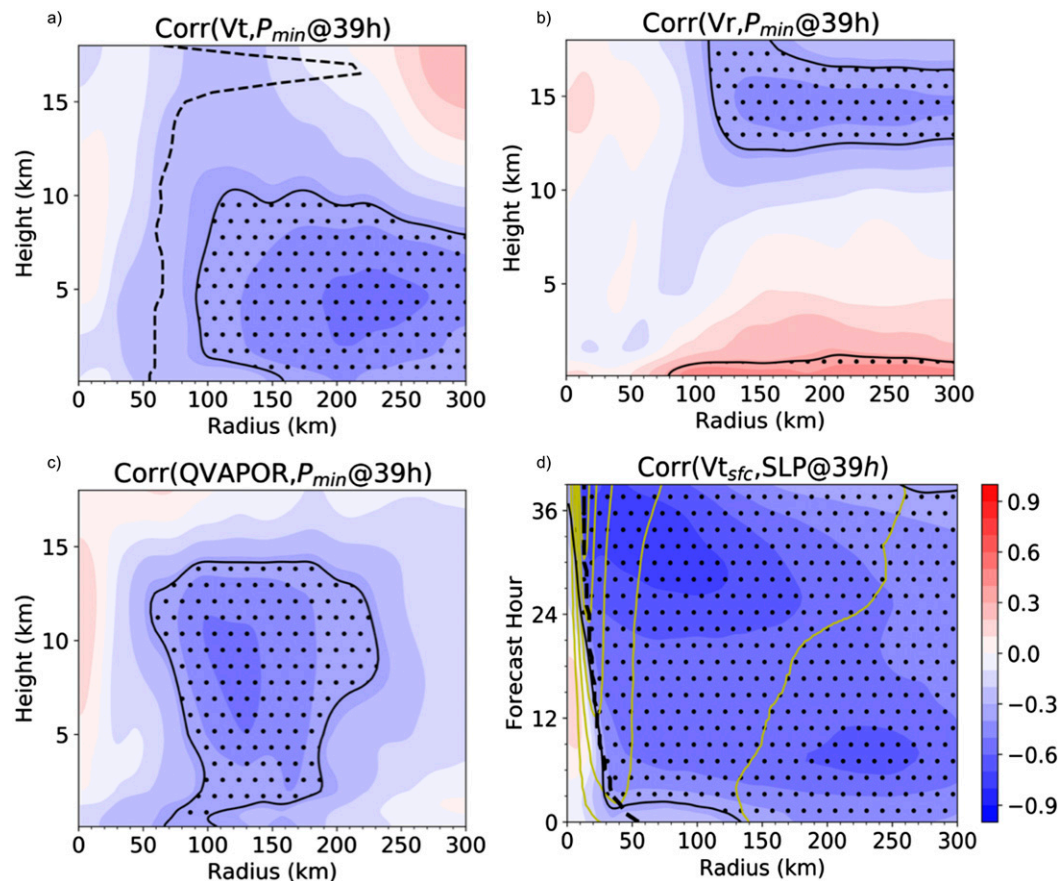


FIG. 8. Ensemble storm-relative radius–height correlations of initial (a) tangential wind speed, (b) radial wind speed, and (c) vapor mixing ratio (QVAPOR) to the minimum central pressure at 39 h, the time of peak estimated intensity. (d) Radius–time Hovmöller of ensemble correlation between azimuthal mean 10-m tangential wind speed and minimum central pressure at 39 h; the azimuthal mean 10-m tangential wind speed is also contoured every 10 m s^{-1} (gold). Stippling denotes regions where the statistical significance exceeds the 99% confidence interval and dashed line in (a),(d) denotes the RMW.

members failed to achieve the observed peak intensity despite being embedded within a favorable environment with some of the lowest vertical wind shear among the ensemble (not shown).

To further examine the potential interplay between the structure of Patricia's outer vortex and an unfavorable environment, experiments are also conducted in which a good vortex (CNTL) is gradually relaxed to a bad environment and outer TC circulation (member 31). When the environment ICs from CNTL are replaced by those of member 31 (e.g., r600bad and r400bad) the vertical wind shear is increased to $\sim 8 \text{ m s}^{-1}$ at its peak (Fig. 9d), but the associated forecasts still reach a peak maximum wind speed nearly identical to CNTL, despite a brief interruption in the rapid intensification from 18 to 24 h—roughly coincident with the peak in vertical wind shear (Figs. 9d,f). When the outer circulation of CNTL is gradually

relaxed to member 31 from 100 to 200 km radii (r200bad) the tangential wind speeds in this region are decreased (Fig. 9e) and the forecasted peak maximum wind speed is $\sim 40 \text{ m s}^{-1}$ less than CNTL (Fig. 9f). The strength of the outer TC circulation beyond the RMW and the environmental vertical wind shear both play important roles in the intensification process and the peak intensity variability across the ensemble.

Furthermore, the negative correlation (~ -0.5) between the initial maximum radius of tropical storm force winds and the minimum central pressure at 39 h indicates a rather robust relationship across the ensemble, where ensemble members with larger outer primary circulations are associated with a more intense storm at the time of peak observed intensity. The ensemble correlation between vertical wind shear and minimum central pressure at 39 h is much weaker at all forecast times (maximum of ~ 0.25 from 18 to 36 h; not

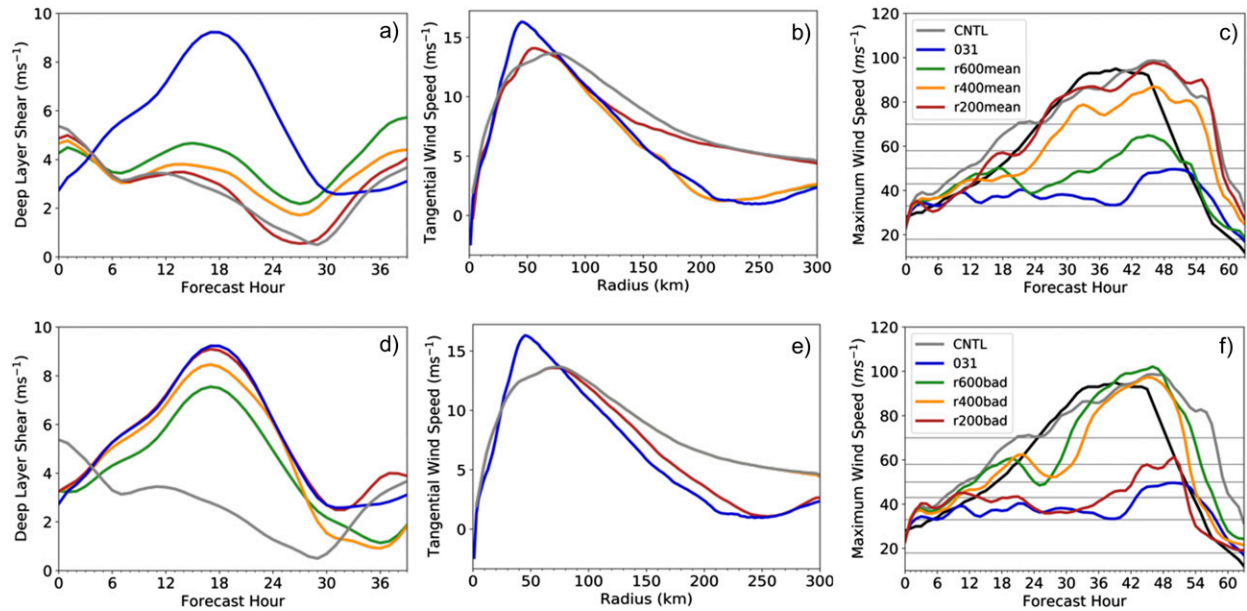


FIG. 9. (a),(d) Deep layer vertical wind shear through 39 h, (b),(e) radial profiles of 10 m tangential wind speed at the initial time, and (c),(f) simulated maximum 10 m wind speed throughout the forecast period. (top) Sensitivity experiments for gradually changing initial conditions from the worst ensemble member (031) to the analysis mean initial conditions (CNTL). (bottom) Sensitivity experiments for gradually changing initial conditions from the analysis mean (CNTL) to initial conditions from the worst ensemble member (031). The best track maximum wind speed is shown as the black curve.

shown), implying that the differences in the size of the TC circulation may determine the amount of vertical wind shear that prevents the TC from rapidly intensifying. A broader and stronger vortex is able to undergo a more Patricia-like intensification, even if embedded within $6\text{--}10\text{ m s}^{-1}$ vertical wind shear, while a smaller and weaker vortex is unable to rapidly intensify like Patricia, even if embedded within 4 m s^{-1} vertical wind shear. We hypothesize that the stronger tangential winds beyond the RMW are important for the intensification of Patricia for at least two reasons. First, the additional angular momentum beyond the RMW can be advected radially inward near the surface and converted into kinetic energy through conservation of angular momentum (e.g., Smith et al. 2009). Second, in agreement with Reasor et al. (2004), broader TCs are believed to be more resilient to vertical wind shear as a result of increased inertial stability.

This ensemble sensitivity analysis also helps to explain the main benefits from the assimilation of airborne radial velocity observations in improving the forecasts of Patricia's intensification process, compared to the assimilation of conventional observations alone. The assimilation of airborne radial velocity helps to better constrain and initialize the structure of the primary and secondary circulation of Patricia at all radii, which allowed the intensification process, timing, and peak

intensity to be better predicted than operational models and CONV.

c. Sensitivity of Patricia's forecasts to model resolution and surface physics parameterization

In this subsection, we would like to provide some brief commentary on the impact of model error on the prediction of Patricia's intensification. In particular, we focus on the impacts of model horizontal grid resolution and the parameterization of the ocean-atmosphere exchange of enthalpy and momentum, which we found to be particularly important in capturing Patricia's intensification.

High-resolution operational guidance available to forecasters for real-time prediction of Patricia (e.g., HWRF) utilized horizontal grid spacing of—at best— $\sim 3\text{ km}$ (Tallapragada et al. 2015), while forecasts shown thus far, on the other hand, have utilized horizontal grid spacing of 1-km for the innermost domain. To investigate the impact of this decreased horizontal grid spacing on the predicted intensity and simulated TC structure, forecasts with 3-km horizontal grid [i.e., without the inner 1-km nested domain (D04)], are initialized from the same Airborne+CONV EnKF analysis mean as before and at two times immediately following the assimilation of airborne radial velocity observations (Figs. 10a,b, 11a-f, and 12a-f). The peak maximum wind speed from the forecast with 3-km horizontal grid spacing is $\sim 16\text{ m s}^{-1}$ less than with 1-km horizontal grid spacing for the forecast initialized from

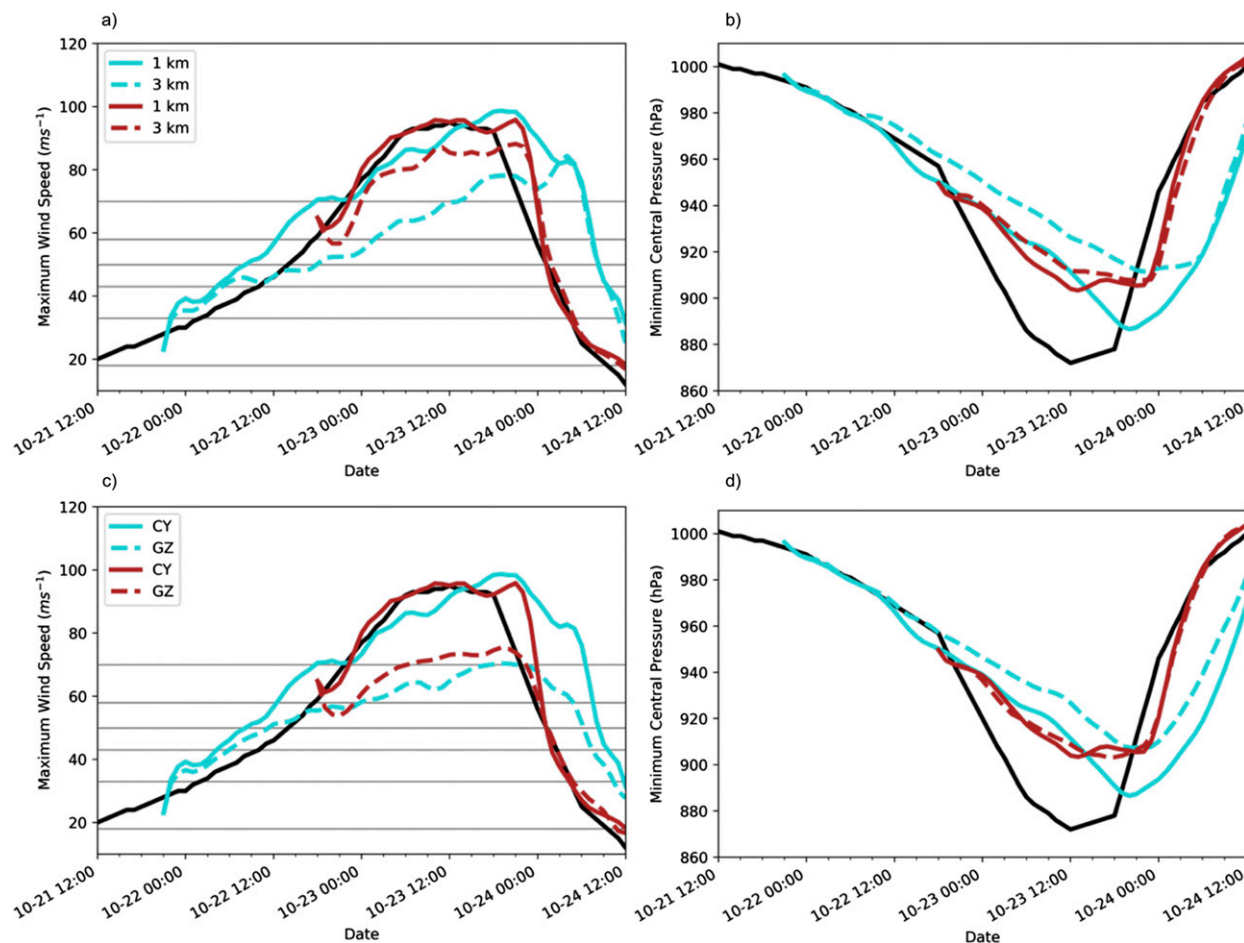


FIG. 10. Deterministic intensity forecasts of (a),(c) maximum wind speed and (b),(d) minimum central pressure initialized from the Airborne+CONV analysis mean at 2100 UTC 21 Oct and 1800 UTC 22 Oct for (top) innermost domain horizontal grid spacing of 1 km (solid) and 3 km (dashed) and (bottom) surface flux parameterization from CY (solid) and GZ (dashed). The best track is shown as the black curve.

2100 UTC 21 October and $\sim 8 \text{ m s}^{-1}$ less for the forecast initialized from 1800 UTC 22 October (Fig. 10a).

For the 3-km forecast from 2100 UTC 21 October, the RMW is increased by as much as 5 km, the primary and secondary circulations are visibly weakened, and the eyewall appears to slope more outward with radius, compared with the 1-km forecast (Figs. 11a–f). The 3- and 1-km forecasts initialized from 1800 UTC 22 October exhibit smaller differences in the maximum surface wind speed (Fig. 10a), tangential wind speed throughout the troposphere, and the RMW (Figs. 12a–c), than the forecast initialized from 2100 UTC 21 October (Figs. 11a–c). However, the RMW is still generally smaller for the 1-km forecast than the 3-km forecast for both initialization times. Differences in the secondary circulation appear more complex in the later forecasts, as the primary differences in the radial inflow at 6 h (Fig. 12d) and 12 h (Fig. 12e) into the forecast appear to be the result of slight differences in the RMW and

therefore the location where the boundary layer radial inflow converges and rises within the eyewall. At 24 h into the forecast, the boundary layer inflow is stronger in the 3-km simulation than the 1-km simulation and differences of more than 5 m s^{-1} are also apparent within the upper-level outflow (Fig. 12f), indicating more of the kinetic energy might have been transported to the primary circulation versus the secondary circulation in the 1-km forecast, since tangential wind speeds are greater in 1 km than 3 km. Overall, the increased horizontal resolution appears important in order to capture Patricia's observed maximum wind speed and small and compact inner core with very tight radial gradients, in agreement with Fox and Judt (2018) and Qin and Zhang (2018). Additionally, the effect of the different horizontal resolutions appears here to be greater for the forecast initiated near the beginning of RI (2100 UTC 21 October) versus the forecast initialized in the middle of the RI (1800 UTC 22 October).

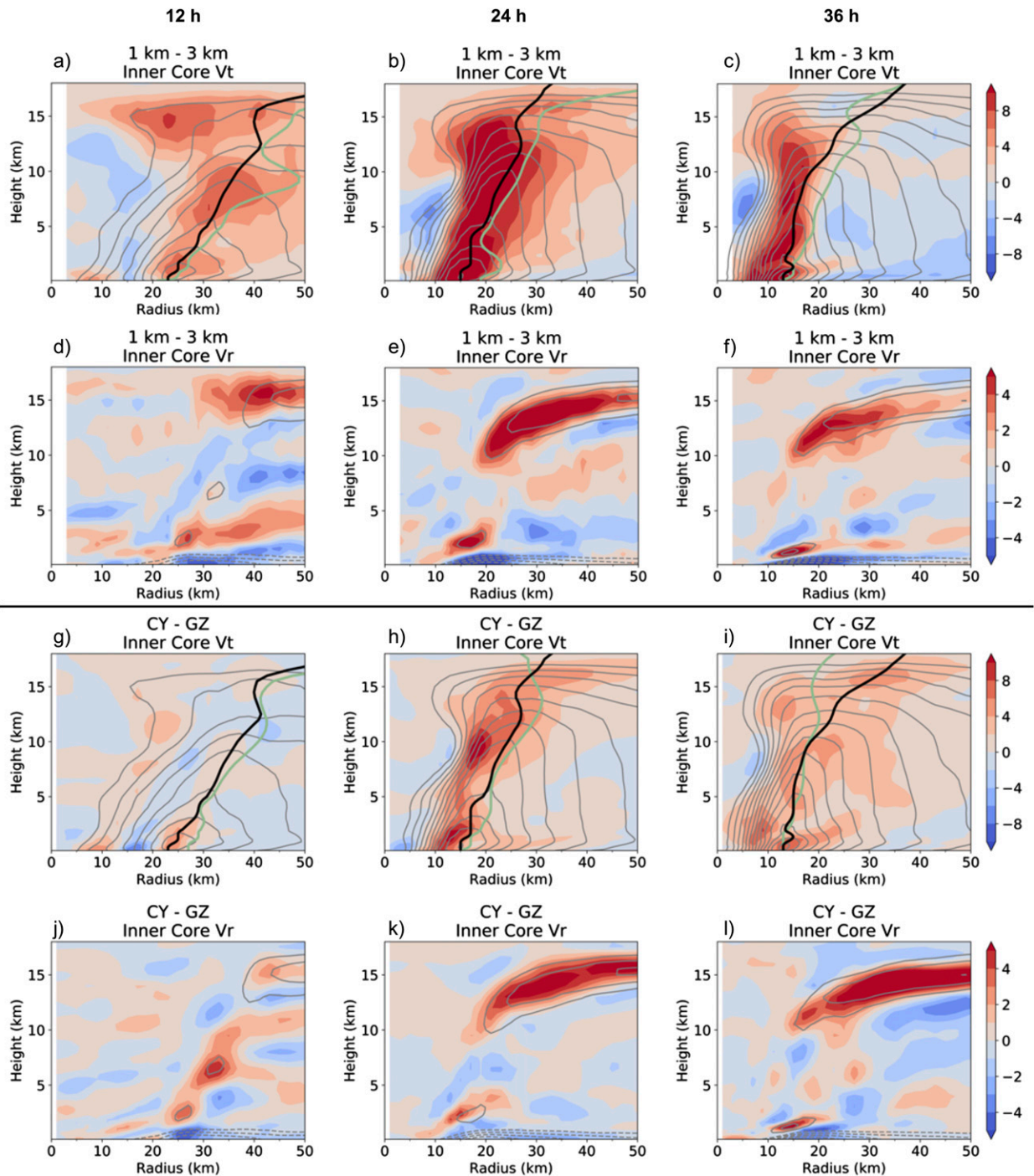


FIG. 11. Storm-relative radius–height difference between (a)–(f) forecasts with 1 and 3 km horizontal grid spacing and (g)–(l) CY and GZ surface flux parameterization are shaded for forecasts initialized from 2100 UTC 21 Oct Airborne+CONV EnKF analysis mean. The radius–height structure of the 1 km CY simulation is contoured for reference in gray every 5 m s^{-1} (starting at 10 m s^{-1}) for the tangential wind and every 4 m s^{-1} for the radial wind (negative radial wind contours are dashed). The RMW in the 1 km or CY simulation is shown by the black line and the RMW in the 3 km or GZ simulation by the green line.

In addition to the impact of model horizontal resolution

for the innermost domain, but with two different parameterizations for the ocean–atmosphere exchange of enthalpy and momentum. The main difference between

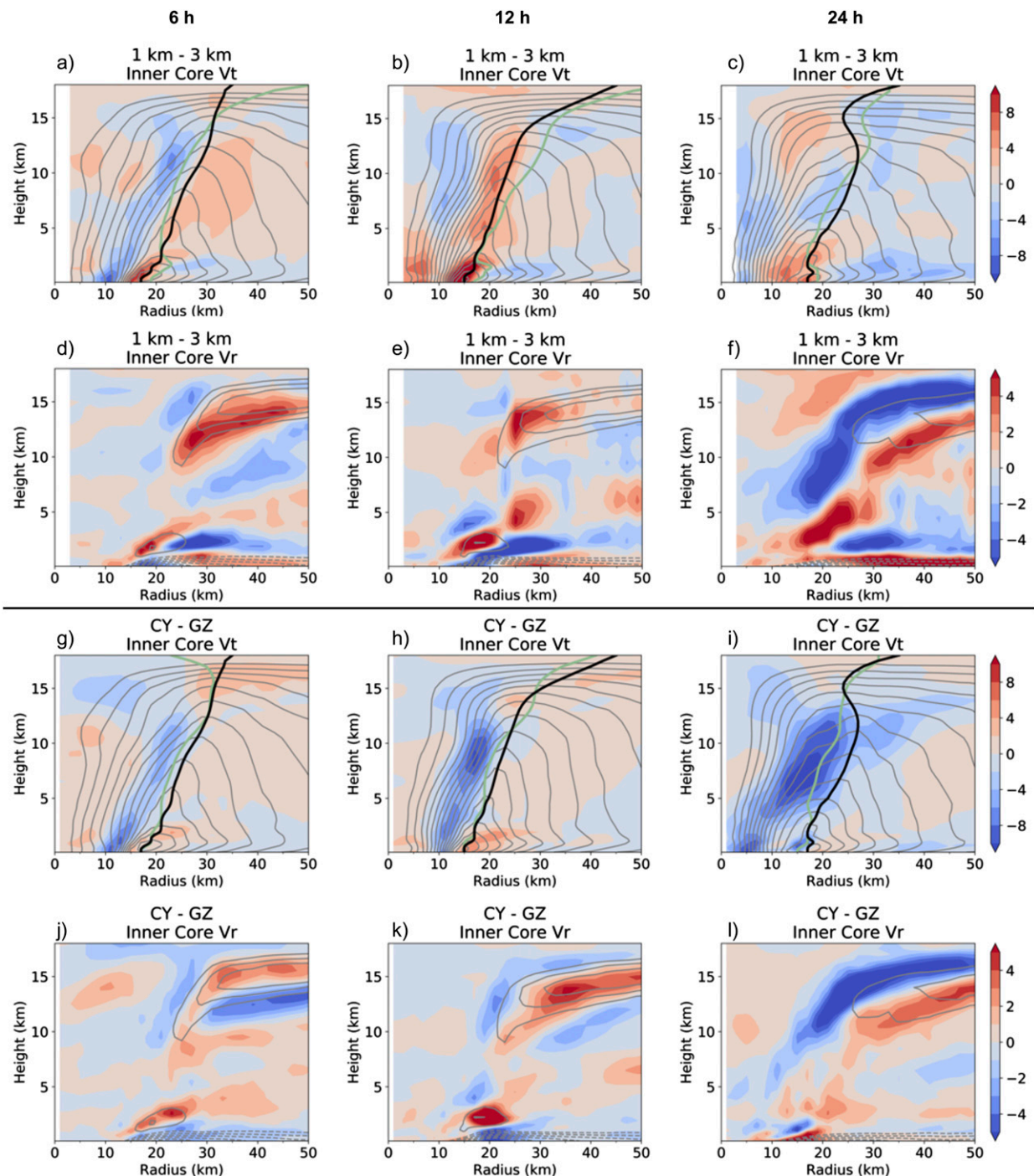


FIG. 12. As in Fig. 11, but forecasts initialized from 1800 UTC 22 Oct.

these two schemes is the surface drag coefficient (C_d) at high wind speeds. The first (CY), from [Chen et al. \(2018\)](#), assumes that C_d decreases with wind speed for wind speeds greater than hurricane force. The second (GZ), from [Green and Zhang \(2013\)](#), has been utilized in the real-time PSU WRF EnKF system and assumes

that C_d gradually increases with wind speed for wind speeds greater than hurricane force. Differences between these two parameterizations are explained in much greater detail in [Chen et al. \(2018\)](#). At the current time, considerable uncertainty exists in the true relationship between the surface drag coefficient and wind

speed for wind speeds greater than hurricane force (33 m s^{-1} ; e.g., Powell et al. 2003; Black et al. 2007; Holthuijsen et al. 2012; Bell et al. 2012; Green and Zhang 2013, 2014; Chen et al. 2018) and we attempt here to examine two extremes of this current uncertainty range.

Uncertainty in the parameterization of the exchange of momentum and enthalpy is shown to greatly change the simulated intensity (Figs. 10c,d) and the inner-core structure (Figs. 11 and 12g–l). Consistent with MPI theory, where the square of the theoretical maximum wind speed is directly proportional to the ratio of C_k and C_d (Emanuel 1995), as C_d is decreased for high wind speeds (CY), relative to GZ, the maximum simulated wind speed is greater. The difference in maximum surface winds between CY and GZ for a 6 h time period around the time of peak intensity is $\sim 27 \text{ m s}^{-1}$ for the forecast initialized from 2100 UTC 21 October and $\sim 21 \text{ m s}^{-1}$ for the forecast initialized from 1800 UTC 22 October, corresponding to an $\sim 25\%$ reduction in the peak surface wind speed in GZ relative to CY. The estimated differences in MPI between CY and GZ using (1) and the appropriate C_k and C_d wind speed relationship from CY and GZ is $\sim 33 \text{ m s}^{-1}$. While the calculated difference from theory is a bit higher than the actual forecast differences, it is possible one or both of the simulated storms have not yet reached their MPI. Despite the relative simplicity of the theory and the somewhat empirical estimations of assumed parameters in the MPI calculation (e.g., the outflow temperature or the enthalpy exchange taking place only at the RMW), we argue that the impact of changes to the surface flux parameterization on forecasts of Patricia can be explained, at least to the first order, by the MPI theory [Eq. (1)], where the square of the maximum wind speed is directly proportional to the ratio of the surface enthalpy coefficient to the surface drag coefficient.

While the most meaningful differences between the two simulations occur within the boundary layer, differences in the vertical structure of the primary and secondary circulations are also apparent and 12 h into the 2100 UTC 21 October forecast, the RMW is $\sim 5 \text{ km}$ smaller in CY than GZ, which is likely a result of the stronger boundary layer inflow in CY that may be acting to spin up the storm more quickly than in GZ (Figs. 11g,j). At 24 h, differences in the RMW are reduced but, overall differences in the primary and secondary circulations have increased, as CY has tangential wind speeds more than 8 m s^{-1} greater than GZ near the eyewall throughout much of the troposphere and the outflow is also stronger in CY at this time by more than 5 m s^{-1} (Figs. 11h,k). By 36 h, differences in the RMW are virtually gone and differences in the tangential wind speed throughout the troposphere are actually less than

seen at 24 h (Figs. 11h,i), despite differences in maximum surface wind speeds continuing to increase during this time (Fig. 10c). Conversely, differences in the secondary circulation increased between 24 and 36 h (Figs. 11k,l).

While intensity differences between the 1-km and 3-km forecasts were reduced for the forecast initialized from 1800 UTC 22 October, relative to the forecast initialized from 2100 UTC 21 October, comparable differences for this forecast are still apparent between CY and GZ (Fig. 10c), as differences in the surface drag coefficient between CY and GZ increase with wind speed for wind speeds greater than hurricane force. The largest differences in the primary circulation between CY and GZ for these forecasts appear to be radially inward of the RMW, perhaps because of the increased surface drag in GZ at high winds resulting in a more upright eyewall (Figs. 12g–i). Additionally, by 24 h into the forecasts, the radial inflow within the boundary layer now appears stronger in GZ than CY, similar to Green and Zhang (2014), and again likely a result of the increased surface drag in GZ at high wind speeds (Fig. 12l).

From the experiments presented in this subsection, it can be seen that both the model horizontal resolution and choice in ocean–atmosphere momentum and enthalpy exchange parameterization can meaningfully impact the prediction of Patricia’s intensification process. Additionally, based on the comparison of simulations with different surface drag formulations shown, the assumption of an increasing drag coefficient at high wind speeds is clearly inappropriate for Hurricane Patricia, and likely other intense tropical cyclones. We expect that uncertainties in other model physical processes and their parameterizations (such as microphysics and boundary layer turbulence) can further limit the prediction skill of this record-breaking storm.

d. Key sources of ensemble forecast error and reduced practical predictability in Patricia’s intensification

The practical predictability of Patricia’s intensification is influenced by a combination of the intrinsic limit, related to the chaotic nature of the atmosphere, IC uncertainty, which is impacted by the data assimilation system and availability of observations, and model uncertainty, such as model physics uncertainty or unresolved forcing. Because by definition the intrinsic limit cannot be further improved, we focus on the impacts of IC and model uncertainties, specifically the model horizontal resolution and physics related to the air–sea fluxes. To place the impacts of IC uncertainty, coarser model horizontal resolution, and a suboptimal surface

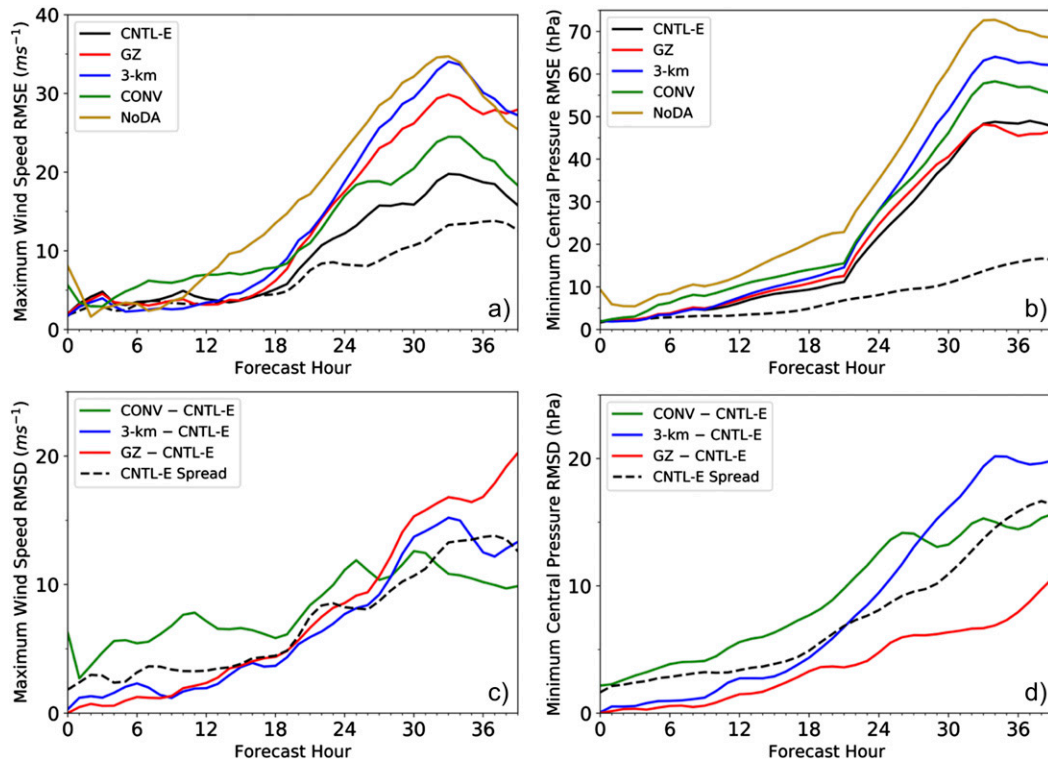


FIG. 13. (top) Root-mean-square error and (bottom) pairwise root-mean-square difference for (left) maximum wind speed and (right) minimum central pressure. Dash black line in all panels depicts the ensemble spread of control ensemble (CNTL-E).

flux parameterization on the forecast accuracy and practical predictability into context, we have conducted several additional sets of 10-member ensemble forecasts initialized from 2100 UTC 21 October with four different model configurations and compared with the corresponding first 10 members from the control Airborne+CONV ensemble (CNTL-E). The impact of IC uncertainty, model resolution, and air-sea flux parameterization on the forecast accuracy is assessed by calculating the ensemble root-mean-squared error (RMSE), relative to best track, and comparing with that of CNTL-E, which has the lowest RMSE (Figs. 13a,b). The impact on predictability is further evaluated by comparing the pairwise root-mean-square difference (RMSD) between the corresponding members of the ensemble with a modified configuration and the subset of the CNTL ensemble (CNTL-E) against the ensemble spread of CNTL-E, which includes only the 10 members used in calculating the pairwise RMSD. By examining the pairwise ensemble RMSD between CNTL-E and a given modified ensemble, we can isolate the forecast uncertainty resulting from specific sources. A pairwise ensemble RMSD greater than the ensemble spread of CNTL-E indicates that the modified ensemble configuration results in differences, relative to CNTL-E,

that are larger than the ensemble spread of CNTL-E and therefore implies that forecast uncertainty grows more rapidly as a result of the modification than that from the IC uncertainty of CNTL-E.

The first ensemble configuration examines the consequences if no data assimilation is performed (NoDA). The ensemble is initialized from GFS with CV3 ensemble perturbations (NoDA), and the model configuration is identical to CNTL-E. NoDA has the largest RMSE of all ensemble configurations shown, and the average RMSE over the first 39 h is more than 74% (99%) greater in terms of maximum wind speed (minimum central pressure) than CNTL-E (Figs. 13a,b), demonstrating that the ensemble data assimilation performed in CNTL-E considerably improved intensity forecasts of Patricia relative to NoDA.

The second ensemble is designed to assess the consequences on the intensity forecast predictability if airborne observations were not available, and therefore only assimilates conventional observations (CONV). The maximum wind speed (minimum central pressure) RMSE for CONV averaged over the first 39 h is more than 40% (37%) greater than CNTL-E (Figs. 13a,b), demonstrating assimilation of airborne radial velocity observations appreciably reduced the intensity forecast

errors over the first 39 h. Additionally, the pairwise RMSD between CNTL-E and CONV is greater than the CNTL-E spread over the first 30 h—by as much as 4.6 m s^{-1} (140%) and 5 hPa (66%)—and comparable over the next 9 h (Figs. 13c,d). The greater pairwise differences between CONV and CNTL-E, than the CNTL-E spread, imply that the CONV ensemble is more different from CNTL-E than CNTL-E members are from each other. Furthermore, the maximum winds speed (minimum central pressure) ensemble spread of CONV is also more than 54% (19%) greater than CNTL-E (not shown), demonstrating increased intensity forecast uncertainty without assimilation of airborne radial velocity observations.

In addition to IC uncertainty, model horizontal resolution and choice in surface flux parameterization have already been shown to degrade deterministic forecasts of Patricia's intensification (Fig. 10). To further assess the impact of model uncertainties from coarser horizontal resolution on the practical predictability, a 10-member ensemble is conducted identical to CNTL-E, but with 3-km horizontal grid spacing for the innermost domain during the forecasts (3 km) (i.e., without the 1-km finest domain used in CNTL-E). The maximum wind speed (minimum central pressure) ensemble RMSE for 3-km averaged between 12 and 39 h is more than 52% (27%) greater than the CNTL-E (Figs. 13a,b), further indicating that inadequate model horizontal resolution can be an important model error source in accurately capturing Patricia's intensification. Additionally, the pairwise ensemble RMSD of Patricia's maximum wind speed (minimum central pressure) beyond 24 h (21 h) is increased, relative to the CNTL-E spread, solely from the difference in horizontal resolution utilized during the forecasts by as much as 3 m s^{-1} or 28% (5.6 hPa or 50%; Figs. 13c,d). The greater pairwise ensemble RMSD between 3-km and CNTL-E, than the CNTL-E spread, indicates that beyond ~ 1 day, intensity forecast uncertainty increases more rapidly from differences in horizontal resolution than from the IC differences of CNTL-E.

Arguably the worst performing deterministic forecasts were from those utilizing a surface drag coefficient which—we speculate erroneously—increased with wind speed (Figs. 10c,d). To further assess the impact of potential errors within the model parameterized surface drag coefficient on intensity forecast errors and ensemble predictability, a 10-member ensemble forecast identical to CNTL-E, but with GZ surface drag formulation (GZ) was performed. The maximum wind speed RMSE, averaged between 24 and 39 h, for GZ is more than 53% greater than CNTL-E, with CY surface drag formulation (Figs. 13a,b). The substantial increase in

ensemble simulated maximum wind speed RMSE, resulting from changes in the surface drag coefficient formulation, highlights the major intensity forecast degradation that is possible for intense TCs if an inadequate surface drag parameterization is used. Additionally, the pairwise ensemble RMSD of Patricia's maximum wind speed between GZ and CNTL-E is increased beyond 21 h, relative to the ensemble spread of CNTL-E, by as much as 7.6 m s^{-1} (60%) at 39 h, as a result of only differences in the surface drag coefficient at high wind speeds (Fig. 13c). The greater pairwise ensemble RMSD for the maximum wind speed between GZ and CNTL-E, than the CNTL-E spread, indicates that beyond ~ 1 day, uncertainty in simulated maximum wind speed increases more rapidly from differences in the surface drag coefficient than the IC differences of CNTL-E. The greatest maximum wind speed RMSD from CNTL-E near the time of peak intensity (39 h), for all ensemble sets shown, is observed in GZ, indicating that the model surface drag formulation uncertainty potentially has a more substantial impact on the uncertainty in simulated peak wind speed of intense TCs, like Patricia, than current IC uncertainty (CNTL-E) or changes from 3- to 1-km horizontal grid spacing. The minimum central pressure on the other hand, is less sensitive to changes in the surface drag (Figs. 13b,d), in agreement with Green and Zhang (2014).

4. Conclusions

Compared with operational guidance present at the time of Hurricane Patricia, the current study examines the potential for improving the practical predictability of Hurricane Patricia's rapid intensification to its peak intensity through assimilating airborne Doppler radar radial velocity observations in the inner core region with an ensemble Kalman filter, reducing horizontal grid spacing of the forecast model, and using an improved surface flux parameterization in which the surface drag decreases with wind speed above hurricane force.

Complementary to previous investigations, it is demonstrated that assimilation of airborne radial velocity observations is crucial to better capture the initial inner-core structure and intensity and to subsequently improve the deterministic and ensemble analyses and forecasts of the hurricane's structure and intensity.

Moreover, using the EnKF analysis perturbations with airborne Doppler observations assimilated, a 60-member ensemble with 1-km horizontal grid spacing demonstrates its ability to simulate the observed maximum wind speed with high probability, since the majority of ensemble members reached at least the observed peak intensity and many capture the observed

record-breaking intensification rate during the forecast, though the timing of reaching the observed peak wind speed was more uncertain. The initial primary and secondary circulations beyond the RMW were found to be the dominant sources of initial condition uncertainty leading to different intensities at the time of peak observed intensity, as members with initially stronger primary and secondary circulations beyond the RMW were able to intensify earlier. Without assimilation of airborne radial velocity observations, ensemble intensity forecast errors are increased by more than 40% and the intensity forecast uncertainty is increased by more than 50%.

Encouragingly but not surprisingly, given the rather compact inner core of Patricia, it is found that the convection-allowing forecasts with 1-km horizontal grid spacing were able to better capture Patricia's structure and reduced ensemble intensity forecast errors by as much as 50%, in comparison with 3-km horizontal grid spacing. This forecast improvement is observed despite the cycling ensemble DA being conducted with a coarser horizontal grid spacing of 3-km. Further systematic expansion of the current investigation to many other tropical cyclone events could lead to the use of real-time prediction using much refined resolution while performing the cycling ensemble DA at the marginal convection-permitting resolution under limited computational constraints. We speculate, based on our limited testing (not shown), that performing the cycling ensemble DA with 1-km horizontal resolution would yield little—if any—improvement because current observations are insufficient spatially and temporally to constrain the uncertainty at the finer resolved scales.

Last, this study demonstrates the importance of not only continuing to reduce IC uncertainty through effective DA methods but also the importance of improvements to numerical models, in particular the parameterization of subgrid-scale physical processes in order to maximize the practical predictability of TCs. In many studies examining TC predictability (e.g., Van Sang et al. 2008; Torn and Cook 2013; Zhang and Tao 2013; Emanuel and Zhang 2016), the model physics uncertainty is often neglected. However, we have demonstrated here that the current physics uncertainty related to the air–sea fluxes can be an important source of intensity forecast uncertainty that is potentially more important than current initial condition uncertainty for prediction of intense tropical cyclones, like Patricia, beyond ~1 day. The very large changes in forecast intensity and structure observed by modifying the air–sea exchange of momentum and enthalpy, demonstrated here and elsewhere (e.g., Green and Zhang 2013, 2014), certainly warrants future research. Specifically, future works are needed to better understand, represent, and

constrain the impact of C_k and C_d uncertainty on TC development, intensification, structure and energetics. Pathways to reduce uncertainty in C_k and C_d , include, but are not limited to, using the budget analysis of Bell et al. (2012), systematic ensemble and parameter sensitivity analysis as in Green and Zhang (2014), and simultaneous state and parameter estimation assimilating in situ and remotely sensed observations (e.g., Aksoy et al. 2006a,b; Hu et al. 2010).

Acknowledgments. This work was supported by NASA Grant 17-EARTH17F-184 under the NASA Earth and Space Science Fellowship Program, and ONR Grants N000141512298 and N000141812517. Computing was conducted at the Texas Advanced Computing Center (TACC) and NOAA Jet Cluster. All modeling and analysis datasets are saved at TACC and can be made freely available upon request. We also wish to acknowledge the NOAA Hurricane Research Division scientists and Aircraft Operation Center flight crew, as well as the scientists and crew of the TCI field campaign, for their data collection. All conventional observations were obtained from the NCAR RDA (<https://rda.ucar.edu/datasets/ds461.0> and <https://rda.ucar.edu/datasets/ds351.0>). Last, we thank three anonymous reviewers for comments that helped to significantly improve the quality of this manuscript.

REFERENCES

- Aberson, S. D., A. Aksoy, K. J. Sellwood, T. Vukicevic, and Z. Zhang, 2015: Assimilation of high-resolution tropical cyclone observations with an ensemble Kalman filter using HEDAS: Evaluation of 2008–11 HWRF forecasts. *Mon. Wea. Rev.*, **143**, 511–523, <https://doi.org/10.1175/MWR-D-14-00138.1>.
- Aksoy, A., F. Zhang, and J. W. Nielsen-Gammon, 2006a: Ensemble-based simultaneous state and parameter estimation with MM5. *Geophys. Res. Lett.*, **33**, L12801, <https://doi.org/10.1029/2006GL026186>.
- , —, and —, 2006b: Ensemble-based simultaneous state and parameter estimation in a two-dimensional sea breeze model. *Mon. Wea. Rev.*, **134**, 2951–2970, <https://doi.org/10.1175/MWR3224.1>.
- Barker, D. M., W. Huang, Y. R. Guo, A. J. Bourgeois, and Q. N. Xiao, 2004: A three-dimensional variational data assimilation system for MM5: Implementation and initial results. *Mon. Wea. Rev.*, **132**, 897–914, [https://doi.org/10.1175/1520-0493\(2004\)132<0897:ATVDAS>2.0.CO;2](https://doi.org/10.1175/1520-0493(2004)132<0897:ATVDAS>2.0.CO;2).
- Bell, M. M., M. T. Montgomery, and K. A. Emanuel, 2012: Air–sea enthalpy and momentum exchange at major hurricane wind speeds observed during CBLAST. *J. Atmos. Sci.*, **69**, 3197–3222, <https://doi.org/10.1175/JAS-D-11-0276.1>.
- , and Coauthors, 2016: ONR tropical cyclone intensity 2015 NASA WB-57 HDSS dropsonde data, version 1.0. UCAR/NCAR–Earth Observing Laboratory, accessed 1 October 2017, <https://doi.org/10.5065/D6KW5D8M>.

- Black, P. G., and Coauthors, 2007: Air–sea exchange in hurricanes: Synthesis of observations from the Coupled Boundary Layer Air–Sea Transfer Experiment. *Bull. Amer. Meteor. Soc.*, **88**, 357–374, <https://doi.org/10.1175/BAMS-88-3-357>.
- Bosart, L. F., P. P. Papin, A. S. Levine, and A. M. Bentley, 2017: Did Gap Flow Associated with a Precursor Central American Gyre Contribute to the Formation of Hurricane Patricia (2015)? *Eighth Northeast Tropical Meteorology Workshop*, Rensselaerville, NY, University at Albany, State University of New York, Session 4.
- Brown, B. R., and G. J. Hakim, 2013: Variability and predictability of a three-dimensional hurricane in statistical equilibrium. *J. Atmos. Sci.*, **70**, 1806–1820, <https://doi.org/10.1175/JAS-D-12-0112.1>.
- Cangialosi, J. P., 2018: National Hurricane Center forecast verification report: 2017 hurricane season. NOAA/NHC, 73 pp., https://www.nhc.noaa.gov/verification/pdfs/Verification_2017.pdf.
- Chen, Y., and C. Snyder, 2007: Assimilating vortex position with an ensemble Kalman filter. *Mon. Wea. Rev.*, **135**, 1828–1845, <https://doi.org/10.1175/MWR3351.1>.
- , F. Zhang, B. W. Green, and X. Yu, 2018: Impacts of ocean cooling and reduced drag on Hurricane Katrina (2005) based on numerical simulations. *Mon. Wea. Rev.*, **146**, 287–306, <https://doi.org/10.1175/MWR-D-17-0170.1>.
- Davis, C., and Coauthors, 2008: Prediction of Landfalling hurricanes with the Advanced Hurricane WRF Model. *Mon. Wea. Rev.*, **136**, 1990–2005, <https://doi.org/10.1175/2007MWR2085.1>.
- Doyle, J. J., and Coauthors, 2017: A view of tropical cyclones from above: The Tropical Cyclone Intensity Experiment. *Bull. Amer. Meteor. Soc.*, **98**, 2113–2134, <https://doi.org/10.1175/BAMS-D-16-0055.1>.
- Emanuel, K. A., 1995: Sensitivity of tropical cyclones to surface exchange coefficients and a revised steady-state model incorporating eye dynamics. *J. Atmos. Sci.*, **52**, 3969–3976, [https://doi.org/10.1175/1520-0469\(1995\)052<3969:SOTCTS>2.0.CO;2](https://doi.org/10.1175/1520-0469(1995)052<3969:SOTCTS>2.0.CO;2).
- , and F. Zhang, 2016: On the predictability and error sources of tropical cyclone intensity forecasts. *J. Atmos. Sci.*, **73**, 3739–3747, <https://doi.org/10.1175/JAS-D-16-0100.1>.
- , and —, 2017: The role of inner-core moisture in tropical cyclone predictability and practical forecast skill. *J. Atmos. Sci.*, **74**, 2315–2324, <https://doi.org/10.1175/JAS-D-17-0008.1>.
- Finocchio, P. M., and S. J. Majumdar, 2017: The predictability of idealized tropical cyclones in environments with time-varying vertical wind shear. *J. Adv. Model. Earth Syst.*, **9**, 2836–2862, <https://doi.org/10.1002/2017MS001168>.
- Foltz, G. R., and K. Balaguru, 2016: Prolonged El Niño conditions in 2014–2015 and the rapid intensification of Hurricane Patricia in the eastern Pacific. *Geophys. Res. Lett.*, **43**, 10 347–10 355, <https://doi.org/10.1002/2016GL070274>.
- Fox, K. R., and F. Judt, 2018: A numerical study on the extreme intensification of Hurricane Patricia (2015). *Wea. Forecasting*, **33**, 989–999, <https://doi.org/10.1175/WAF-D-17-0101.1>.
- Green, B. W., and F. Zhang, 2013: Impacts of air–sea flux parameterizations on the intensity and structure of tropical cyclones. *Mon. Wea. Rev.*, **141**, 2308–2324, <https://doi.org/10.1175/MWR-D-12-00274.1>.
- , and —, 2014: Sensitivity of tropical cyclone simulations to parametric uncertainties in air–sea fluxes and implications for parameter estimation. *Mon. Wea. Rev.*, **142**, 2290–2308, <https://doi.org/10.1175/MWR-D-13-00208.1>.
- Hakim, G. J., 2013: The variability and predictability of axisymmetric hurricanes in statistical equilibrium. *J. Atmos. Sci.*, **70**, 993–1005, <https://doi.org/10.1175/JAS-D-12-0188.1>.
- Holthuijsen, L. H., M. D. Powell, and J. D. Pietrzak, 2012: Wind and waves in extreme hurricanes. *J. Geophys. Res.*, **117**, C09003, <https://doi.org/10.1029/2012JC007983>.
- Hsu, J.-Y., R.-C. Lien, E. A. D’Asaro, and T. B. Sanford, 2017: Estimates of surface wind stress and drag coefficients in Typhoon Megi. *J. Phys. Oceanogr.*, **47**, 545–565, <https://doi.org/10.1175/JPO-D-16-0069.1>.
- Hu, X.-M., F. Zhang, and J. W. Nielsen-Gammon, 2010: Ensemble-based simultaneous state and parameter estimation for treatment of mesoscale model error: A real-data study. *Geophys. Res. Lett.*, **37**, L08802, <https://doi.org/10.1029/2010GL043017>.
- Huang, H.-C., J. Boucharel, I.-I. Lin, F.-F. Jin, C.-C. Lien, and I.-F. Pun, 2017: Air–sea fluxes for Hurricane Patricia (2015): Comparison with Supertyphoon Haiyan (2013) and under different ENSO conditions. *J. Geophys. Res. Oceans*, **122**, 6076–6089, <https://doi.org/10.1002/2017JC012741>.
- Jin, H., M. S. Peng, Y. Jin, and J. D. Doyle, 2014: An evaluation of the impact of horizontal resolution on tropical cyclone predictions using COAMPS-TC. *Wea. Forecasting*, **29**, 252–269, <https://doi.org/10.1175/WAF-D-13-00054.1>.
- Judt, F., S. S. Chen, and J. Berner, 2016: Predictability of tropical cyclone intensity: Scale-dependent forecast error growth in high-resolution stochastic kinetic-energy backscatter ensembles. *Quart. J. Roy. Meteor. Soc.*, **142**, 43–57, <https://doi.org/10.1002/qj.2626>.
- Kieu, C. Q., and Z. Moon, 2016: Hurricane intensity predictability. *Bull. Amer. Meteor. Soc.*, **97**, 1847–1857, <https://doi.org/10.1175/BAMS-D-15-00168.1>.
- Kimberlain, T. B., E. S. Blake, and J. P. Cangialosi, 2016: National Hurricane Center tropical cyclone report: Hurricane Patricia (20–24 October 2015). NOAA/NHC Tech. Rep. EP202015, NOAA/NHC, 32 pp., https://www.nhc.noaa.gov/data/tcr/EP202015_Patricia.pdf.
- Majumdar, S. J., M. J. Brennan, and K. Howard, 2013: The impact of dropwindsonde and supplemental rawinsonde observations on track forecasts for Hurricane Irene (2011). *Wea. Forecasting*, **28**, 1385–1403, <https://doi.org/10.1175/WAF-D-13-00018.1>.
- Martinez, J., M. M. Bell, R. F. Rogers, and J. D. Doyle, 2019: Axisymmetric potential vorticity evolution of Hurricane Patricia (2015). *J. Atmos. Sci.*, **76**, 2043–2063, <https://doi.org/10.1175/JAS-D-18-0373.1>.
- Melhauser, C., F. Zhang, Y. Weng, Y. Jin, H. Jin, and Q. Zhao, 2017: A multiple-model convection-permitting ensemble examination of the probabilistic prediction of tropical cyclones: Hurricane Sandy (2012) and Edouard (2014). *Wea. Forecasting*, **32**, 665–688, <https://doi.org/10.1175/WAF-D-16-0082.1>.
- Munsell, E. B., F. Zhang, S. A. Braun, J. A. Sippel, and A. C. Didlake, 2018: The inner-core temperature structure of Hurricane Edouard (2014): Observations and ensemble variability. *Mon. Wea. Rev.*, **146**, 135–155, <https://doi.org/10.1175/MWR-D-17-0095.1>.
- Nystrom, R. G., F. Zhang, E. B. Munsell, S. A. Braun, J. A. Sippel, Y. Weng, and K. A. Emanuel, 2018: Predictability and dynamics of Hurricane Joaquin (2015) explored through convection-permitting ensemble sensitivity experiments. *J. Atmos. Sci.*, **75**, 401–424, <https://doi.org/10.1175/JAS-D-17-0137.1>.
- Poterjoy, J., and F. Zhang, 2016: Comparison of hybrid four-dimensional data assimilation methods with and without the tangent linear and adjoint models for predicting the life cycle of Hurricane Karl (2010). *Mon. Wea. Rev.*, **144**, 1449–1468, <https://doi.org/10.1175/MWR-D-15-0116.1>.

- , —, and Y. Weng, 2014: The effects of sampling errors on the EnKF assimilation of inner-core hurricane observations. *Mon. Wea. Rev.*, **142**, 1609–1630, <https://doi.org/10.1175/MWR-D-13-00305.1>.
- Powell, M. D., P. J. Vickery, and T. A. Reinhold, 2003: Reduced drag coefficient for high wind speeds in tropical cyclones. *Nature*, **422**, 279–283, <https://doi.org/10.1038/nature01481>.
- Qin, N., and D.-L. Zhang, 2018: On the extraordinary intensification of Hurricane Patricia (2015). Part I: Numerical experiments. *Wea. Forecasting*, **33**, 1205–1224, <https://doi.org/10.1175/WAF-D-18-0045.1>.
- Reasor, P. D., M. T. Montgomery, and L. D. Grasso, 2004: A new look at the problem of tropical cyclones in vertical shear flow: Vortex resiliency. *J. Atmos. Sci.*, **61**, 3–22, [https://doi.org/10.1175/1520-0469\(2004\)061<0003:ANLATP>2.0.CO;2](https://doi.org/10.1175/1520-0469(2004)061<0003:ANLATP>2.0.CO;2).
- Rogers, R. F., and Coauthors, 2017: Rewriting the tropical record books: The extraordinary intensification of Hurricane Patricia (2015). *Bull. Amer. Meteor. Soc.*, **98**, 2091–2112, <https://doi.org/10.1175/BAMS-D-16-0039.1>.
- Rotunno, R., and K. A. Emanuel, 1987: An air–sea interaction theory for tropical cyclones. Part II: Evolutionary study using a nonhydrostatic axisymmetric numerical model. *J. Atmos. Sci.*, **44**, 542–561, [https://doi.org/10.1175/1520-0469\(1987\)044<0542:AAITFT>2.0.CO;2](https://doi.org/10.1175/1520-0469(1987)044<0542:AAITFT>2.0.CO;2).
- Sippel, J. A., and F. Zhang, 2008: A probabilistic analysis of the dynamics and predictability of tropical cyclogenesis. *J. Atmos. Sci.*, **65**, 3440–3459, <https://doi.org/10.1175/2008JAS2597.1>.
- Skamarock, W. C., and Coauthors, 2008: description of the Advanced Research WRF version 3. NCAR Tech. Note NCAR/TN-475+STR, 113 pp., <https://doi.org/10.5065/D68S4MVH>.
- Smith, R. K., M. T. Montgomery, and N. Van Sang, 2009: Tropical cyclone spin-up revisited. *Quart. J. Roy. Meteor. Soc.*, **135**, 1321–1335, <https://doi.org/10.1002/qj.428>.
- Stern, D. P., and F. Zhang, 2016: The warm-core structure of Hurricane Earl (2010). *J. Atmos. Sci.*, **73**, 3305–3328, <https://doi.org/10.1175/JAS-D-15-0328.1>.
- Tallapragada, V., and Coauthors, 2015: Hurricane Weather Research and Forecasting (HWRF) Model: 2015 scientific documentation. Developmental Testbed Center, 113 pp., https://dtcenter.org/HurrWRF/users/docs/scientific_documents/HWRF_v3.7a_SD.pdf.
- Tao, D., and F. Zhang, 2014: Effect of environmental shear, sea-surface temperature, and ambient moisture on the formation and predictability of tropical cyclones: An ensemble-mean perspective. *J. Adv. Model. Earth Syst.*, **6**, 384–404, <https://doi.org/10.1002/2014MS000314>.
- Torn, R. D., 2016: Evaluation of atmospheric and ocean initial condition uncertainty and stochastic exchange coefficients on ensemble tropical cyclone intensity forecasts. *Mon. Wea. Rev.*, **144**, 3487–3506, <https://doi.org/10.1175/MWR-D-16-0108.1>.
- , and G. J. Hakim, 2009: Ensemble data assimilation applied to RAINEX observations of Hurricane Katrina (2005). *Mon. Wea. Rev.*, **137**, 2817–2829, <https://doi.org/10.1175/2009MWR2656.1>.
- , and D. Cook, 2013: The role of vortex and environment errors in genesis forecasts of Hurricane Danielle and Karl (2010). *Mon. Wea. Rev.*, **141**, 232–251, <https://doi.org/10.1175/MWR-D-12-00086.1>.
- Van Sang, N., R. K. Smith, and M. T. Montgomery, 2008: Tropical-cyclone intensification and predictability in three dimensions. *Quart. J. Roy. Meteor. Soc.*, **134**, 563–582, <https://doi.org/10.1002/qj.235>.
- Weng, Y., and F. Zhang, 2012: Assimilating airborne Doppler radar observations with an ensemble Kalman filter for convection-permitting hurricane initialization and prediction: Katrina (2005). *Mon. Wea. Rev.*, **140**, 841–859, <https://doi.org/10.1175/2011MWR3602.1>.
- , and —, 2016: Advances in convection-permitting tropical cyclone analysis and prediction through EnKF assimilation of reconnaissance aircraft observations. *J. Meteor. Soc. Japan*, **94**, 345–358, <https://doi.org/10.2151/jmsj.2016-018>.
- Zhang, F., and D. Tao, 2013: Effects of vertical wind shear on the predictability of tropical cyclones. *J. Atmos. Sci.*, **70**, 975–983, <https://doi.org/10.1175/JAS-D-12-0133.1>.
- , and Y. Weng, 2015: Predicting hurricane intensity and associated hazards: A five-year real-time forecast experiment with assimilation of airborne Doppler radar observations. *Bull. Amer. Meteor. Soc.*, **96**, 25–33, <https://doi.org/10.1175/BAMS-D-13-00231.1>.
- , C. Snyder, and J. Sun, 2004: Impacts of initial estimate and observation availability on convective-scale data assimilation with an ensemble Kalman filter. *Mon. Wea. Rev.*, **132**, 1238–1253, [https://doi.org/10.1175/1520-0493\(2004\)132<1238:IOIEAO>2.0.CO;2](https://doi.org/10.1175/1520-0493(2004)132<1238:IOIEAO>2.0.CO;2).
- Zhang, H., and Z. Pu, 2014: Influence of assimilating surface observations on numerical prediction of landfalls of Hurricane Katrina (2005) with an ensemble Kalman filter. *Mon. Wea. Rev.*, **142**, 2915–2934, <https://doi.org/10.1175/MWR-D-14-00014.1>.